



HAL
open science

Martian water vapor: Mars Express PFS/LW observations

T. Fouchet, E. Lellouch, N.I. Ignatiev, François Forget, D.V. Titov, M. Tschimmel, Franck Montmessin, V. Formisano, M. Giuranna, A. Maturilli, et al.

► **To cite this version:**

T. Fouchet, E. Lellouch, N.I. Ignatiev, François Forget, D.V. Titov, et al.. Martian water vapor: Mars Express PFS/LW observations. *Icarus*, 2007, 190 (1), pp.32-49. 10.1016/j.icarus.2007.03.003 . hal-00499071

HAL Id: hal-00499071

<https://hal.science/hal-00499071>

Submitted on 9 Jul 2010

HAL is a multi-disciplinary open access archive for the deposit and dissemination of scientific research documents, whether they are published or not. The documents may come from teaching and research institutions in France or abroad, or from public or private research centers.

L'archive ouverte pluridisciplinaire **HAL**, est destinée au dépôt et à la diffusion de documents scientifiques de niveau recherche, publiés ou non, émanant des établissements d'enseignement et de recherche français ou étrangers, des laboratoires publics ou privés.

Accepted Manuscript

Martian water vapor : Mars Express PFS/LW observations

T. Fouchet, E. Lellouch, N.I. Ignatiev, F. Forget, D.V. Titov,
M. Tschimmel, F. Montmessin, V. Formisano, M. Giuranna,
A. Maturilli, T. Encrenaz

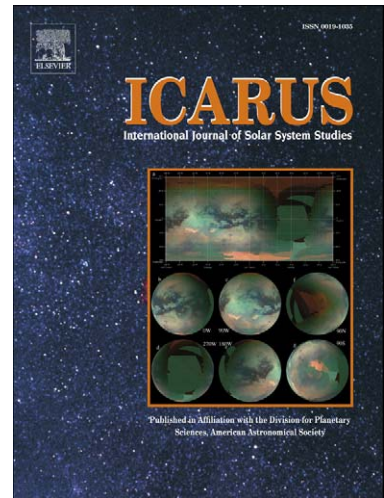
PII: S0019-1035(07)00104-2
DOI: [10.1016/j.icarus.2007.03.003](https://doi.org/10.1016/j.icarus.2007.03.003)
Reference: YICAR 8211

To appear in: *Icarus*

Received date: 9 November 2006
Revised date: 26 February 2007
Accepted date: 5 March 2007

Please cite this article as: T. Fouchet, E. Lellouch, N.I. Ignatiev, F. Forget, D.V. Titov, M. Tschimmel, F. Montmessin, V. Formisano, M. Giuranna, A. Maturilli, T. Encrenaz, Martian water vapor : Mars Express PFS/LW observations, *Icarus* (2007), doi: [10.1016/j.icarus.2007.03.003](https://doi.org/10.1016/j.icarus.2007.03.003)

This is a PDF file of an unedited manuscript that has been accepted for publication. As a service to our customers we are providing this early version of the manuscript. The manuscript will undergo copyediting, typesetting, and review of the resulting proof before it is published in its final form. Please note that during the production process errors may be discovered which could affect the content, and all legal disclaimers that apply to the journal pertain.



Martian water vapor : Mars Express PFS/LW observations

T. Fouchet^{a,b}, E. Lellouch^a, N. I. Ignatiev^{c,d}, F. Forget^e,
D. V. Titov^{c,d}, M. Tschimmel^c, F. Montmessin^f, V.
Formisano^g, M. Giuranna^g, A. Maturilli^g, T. Encrenaz^a

^a Observatoire de Paris, LESIA, Meudon, F-92195, France

^b Université Pierre et Marie Curie - Paris 6, UMR 8109, Paris, F-75005,
France

^cMPS, 37191 Katlenburg-Lindau, Germany

^dSpace Research Institute (IKI), Moscow, Russia

^e Institut Pierre Simon Laplace, LMD, Paris, F-75005, France

^f Institut Pierre Simon Laplace, SA, Verrières-le-Buisson, F-91371,
France

^gIFSI-INAF, Via del Fosso del Cavaliere 100, 00133 Roma, Italy

52 pages

1 table

12 figures

Send correspondence to :

Thierry Fouchet
Observatoire de Paris
LESIA - Bâtiment 17
5 Place Jules Janssen
92195 Meudon Cedex
France

Proposed running head : Mars water cycle from Mars Express/PFS-LW

Abstract

We present the seasonal and geographical variations of the Martian water vapor monitored from the Planetary Fourier Spectrometer Long Wavelength Channel aboard the Mars Express spacecraft. Our dataset covers one Martian year (end of Mars Year 26, Mars Year 27), but the seasonal coverage is far from complete. The seasonal and latitudinal behavior of the water vapor is globally consistent with previous datasets, Viking Orbiter Mars Atmospheric Water Detectors (MAWD) and Mars Global Surveyor Thermal Emission Spectrometer (MGS/TES), and with simultaneous results obtained from other Mars Express instruments, OMEGA and SPICAM. However, our absolute water columns are lower and higher by a factor of 1.5 than the values obtained by TES and SPICAM respectively. In particular, we retrieve a northern midsummer maximum of 60 pr- μm , lower than the 100-pr- μm observed by TES. The geographical distribution of water exhibits two local maxima at low latitudes, located over Tharsis and Arabia. Global Climate Model (GCM) simulations suggest that these local enhancements are controlled by atmospheric dynamics. During Northern spring, we observe a bulge of water vapor over the seasonal polar cap edge, consistent with the northward transport of water from the retreating seasonal cap to the permanent polar cap. In terms of vertical distribution, we find that the water volume mixing ratio over the large volcanos remains constant with the surface altitude within a factor of two. However, on the whole dataset we find that the water column, normalized to a fixed pressure, is anti-correlated with the surface pressure, indicating a vertical distribution intermediate between control by atmospheric saturation and confinement to a surface layer. This anti-correlation is not reproduced by GCM simulations of the water cycle, which do not include exchange between atmospheric and subsurface water. This situation suggests a possible role for regolith-atmosphere exchange in the Martian water cycle.

Keywords: Mars, atmosphere; Mars, climate; Atmospheres, composition

1 Introduction

Along with the cycles of pressure and dust, the water cycle is a key element of the Martian climate, involving interactions between atmospheric reservoirs (water vapor, clouds) and surface reservoirs (polar caps, surface and perhaps subsurface frosts). Since its initial discovery from the ground at $0.82 \mu\text{m}$ (Spinrad et al., 1963), Martian water vapor has been the subject of numerous telescopic observations at visible (Rizk et al., 1991; Sprague et al., 1996, 2001, 2003, 2006), near-infrared (Barker et al., 1970, 1976; Novak et al., 2002), thermal infrared (Lellouch et al., 2000; Burgdorf et al., 2000; Encrenaz et al., 2005a), and millimeter/submillimeter wavelengths (Clancy et al., 1992, 1996; Encrenaz et al., 1991, 1995; Gurwell et al., 2000, 2005; Biver et al., 2005). In general, however, Earth-based observations have not been systematic enough to provide a global view of the seasonal cycle of water (i.e. the variation of water with latitude and season), and the climatology of Mars' atmospheric water is primarily based on spacecraft-borne measurements. After some results in the polar regions by IRIS/Mariner 9 (Conrath et al., 1973; Ignatiev et al., 2002), the first spatially and temporally complete picture of the seasonal behavior of water was established from Viking/MAWD observations of H_2O at $1.38 \mu\text{m}$ from June 1976 through April 1979 (Farmer et al., 1977; Jakosky and Farmer 1982; Jakosky 1985; Jakosky and Haberle 1992; Fedorova et al., 2004). The Viking/MAWD results, which evidenced, in particular, the Northern Polar Cap as the primary source of atmospheric water and a strong North-South asymmetry in the abundance of water, remained the prime observational reference until the operation of MGS/TES in 1999-2004 (Smith, 2002, 2004), although partial results on the geographical and vertical behavior of water were obtained in-between from Phobos in 1989 (Rosenqvist et al., 1992; Titov et al., 1994; Rodin et al., 1997; Titov, 2002) and Pathfinder in 1997 (Titov et al., 1999). The strengths of the MGS/TES water database include (i) its completeness over more than 2 Martian years (ii) its ability to provide simultaneous measurements of the thermal profile, dust loading, and water ice optical depth (iii) the insensitivity of the water vapor measurements to the amount of atmospheric dust. For

these reasons, the TES results on the water cycle have become the usual standard on which modern Martian water climatology is based. The TES annual cycle of water vapor presents a maximum in column abundance at high latitudes during midsummer in both hemispheres, reaching a maximum of ~ 100 $\text{pr-}\mu\text{m}$ in the north, and ~ 50 $\text{pr-}\mu\text{m}$ in the south. Low water abundances are observed during fall and winter at middle and high latitudes of both hemispheres. TES observations and General Climate Models (Montmessin et al., 2004) indicate that water from the southern summer maximum is transported across the equator to the northern hemisphere more efficiently than water from the northern summer maximum to the southern hemisphere.

The water cycle was also a prime objective of the Mars Express mission, with three instruments able to measure the atmospheric water vapor content, either in the solar reflected or in the thermal component. The infrared mapping spectrometer OMEGA provides maps of water from the $2.56 \mu\text{m}$ band with high spatial and low spectral resolution. The infrared spectrometer SPICAM measures water in the $1.38 \mu\text{m}$ band with a 3.5 cm^{-1} spectral resolution (Fedorova et al., 2006). Finally, the PFS instrument, which consists of two channels (long-wavelength and short-wavelength) covering altogether the $1.2\text{--}40 \mu\text{m}$ range, potentially provides measurements of water vapor both in its rotational lines (similar to TES), and in its 2.56 and $1.38 \mu\text{m}$ bands, and giving redundancy with OMEGA and SPICAM. Besides the complementarity of its instrumentation, one advantage of Mars Express with respect to the problem of the water cycle is its quasi-polar orbit, allowing in particular a detailed view of the polar caps at the sublimation onset, as already exploited by OMEGA (Encrenaz et al., 2005b; Melchiorri et al., 2006). We here report on results obtained on the long-wavelength channel of PFS.

2 Instrument and observations description

2.1 The Planetary Fourier Spectrometer

The Planetary Fourier Spectrometer is an infrared double-pendulum interferometer working in two different channels. The short wavelength channel (SWC) covers wavenumbers from 1700 to 8200 cm^{-1} (1.2–5.9 μm) while the long wavelength channel (LWC) operates in the range 250–1700 cm^{-1} (5.9–40 μm). In principle, the availability of the two channels makes it possible to measure water in both the thermal and solar reflected components simultaneously. It was hoped (Formisano et al., 2002) that the combination of measurements in the rotational lines and in the 2.56 and 1.38- μm bands would provide a determination of the water vertical profile, a parameter that so far was directly accessible only to submillimeter observations spectrally resolving the individual water lines. However, this objective could not be met. First, the S/N in the PFS spectra turned out to be insufficient to measure water at 1.38 μm except in very large averages. This prevents this band to be used for water vapor mapping. Second, the amounts (column density) of water measured at 2.56 μm appeared to be quantitatively irreconcilable (1.5–3 times larger) with those determined from the rotational lines, although the two datasets generally gave very consistent trends as to the variability of the water vapor content with latitude, season, and altitude. Results from the SWC channel will be presented by Ignatiev et al., currently in preparation. In the present analysis we have used data from LWC. Its detector is a pyroelectric (LiTaO_3) working at a temperature of ~ 287 K. The LWC is characterized by an unapodized spectral resolution of 1.3 cm^{-1} , a sampling step of 1.0 cm^{-1} and a field of view of 50 mrad (FWHM). This corresponds to 12 kilometers on Mars surface when viewed from periapsis. PFS has a scanning device, allowing observation to be performed either in nadir or in side-looking viewing. A more detailed description of the PFS instrument can be found in Formisano et al. (2005).

2.2 Observations

Mars Express orbiter was successfully inserted into Martian orbit on December 25th, 2003 ($L_s = 322^\circ$). The satellite is located on an eccentric quasi-polar orbit (inclination of 86.35°). The periapsis altitude is approximately 250 km, while the periapsis latitude has drifted during the mission from close to equator at the beginning of the mission to over the South Pole in July 2004 (Orbit #523, $L_s = 48.8^\circ$), and then northward to reach the North Pole in April 2005 (Orbit #1536, $L_s = 183.4^\circ$). The spatial resolution obtained at a given latitude hence depends on the orbit or season of the observations. The Mars Express orbiter is not located in a sun-synchronous orbit. For this reason, various local times (LT) have been covered during the mission, ranging from 8 am to 8 pm (Fig. 1). PFS scientific observations started on orbit #10 ($L_s = 331^\circ$).

In orbit, it takes 4.5 seconds to acquire a PFS interferogram, with a repetition time of 8.5 seconds. On average, about 300 spectra on the planet are obtained during an orbit. PFS observations do not take place on each orbit, as the power and telemetry resources of the spacecraft do not allow the whole Mars Express payload to operate simultaneously. In particular, when the Mars Advanced Radar for Subsurface and Ionosphere Sounding (MARSIS) was switched on in May 2005, the other instruments were set off, and no PFS observations were acquired over the next two months ($L_s = 200^\circ$ – 240°). Moreover PFS suffered an internal problem (strong modulation of the laser diode controlling the double pendulum) and ceased scientific observations for a little over 4 months, between July and November 2005. We here present data covering the January 2004 – December 2005 period, encompassing roughly a Martian year, although, for the above reasons, the seasonal coverage by PFS is far from complete.

2.3 Data Calibration

The PFS LW channel calibration has been presented in details by Giuranna et al. (2005). The instrument spectral response function was obtained both from laboratory

measurements and from flight measurements. Laboratory measurements were obtained by looking at a blackbody tunable within a large range of temperatures (170–270 K). In flight radiometric calibration measurements are taken by looking at the internal blackbody and pointing the scanner towards deep space. The response functions derived from laboratory and in flight measurements are in excellent agreement. One difficulty in the calibration process arises from the evolution of the optics temperature during an observation session (the detector temperature remains stable within ± 0.05 K). This evolution is measured by looking at deep space at the beginning and at the end of a session, and then taken into account in the calibration process. Within the wavenumber range of interest for this study (250–850 cm^{-1}), the noise equivalent spectral radiance (NESR) of a single spectrum varies between 7×10^{-8} and 1.5×10^{-7} $\text{W cm}^{-2} \text{sr}^{-1}/\text{cm}^{-1}$ (corresponding to a signal-to-noise ratio of 50–100 on a mid-latitude daytime spectrum).

3 Analysis

The first step in our analysis is the inversion the temperature profile as a function of pressure, which is based on the fitting of the ν_2 band of CO_2 centered at 667 cm^{-1} . Then the water rotational lines in the 250–500 cm^{-1} range is used to retrieve the Martian H_2O vapor column density.

3.1 Forward model

The forward radiative transfer modelling is carried out using a line-by-line model including the gaseous absorptions by CO_2 and H_2O only. The model assumes a plane-parallel geometry and does not take dust scattering into account. The spectroscopic parameters come from the GEISA data base (Jacquinot-Husson et al., 1999), except for the CO_2 -broadening parameters. For water, we use the parameters calculated by Gamache et al. (1995). On average (but not uniformly), the CO_2 -broadened H_2O linewidths are 1.7 times larger than those from the GEISA database, which correspond to broadening by air. However, in con-

trast with Smith (2000), who multiply the N_2 -broadening parameters by a constant factor of 1.5, our approach takes into account the variation of the CO_2 -broadening coefficient depending on the particular transition.

The calculation of a synthetic spectrum for Mars requires to specify the surface pressure, the surface temperature and the surface emissivity. The Martian surface pressure varies strongly as a function of four parameters: season, latitude, longitude and local time. Surface pressure is predicted by interpolating the Viking Lander 1 record vertically using the accurate MOLA topography (Smith et al., 2001a) and horizontally using the meteorological pressure gradients (including the thermal tides) simulated by the LMD Mars General Circulation Model (Hourdin et al., 1993; Forget et al., 1999) which are available from the European Mars Climate Database Version 4.1 (Forget et al., 2006). Note that we do not average the pressure over the PFS FOV. The uncertainty in the calculated surface pressure is estimated to 10–20 Pa. We also note that in principle, the local pressure could have been determined from the PFS spectra by using the $2.0 \mu\text{m}$ band of CO_2 , but this band appeared to be unusable due to strong spectral perturbations in the SWC channel associated with instrumental problems and spacecraft vibrations.

In the forward calculation, the surface temperature is specified to be the mean of the brightness temperature in the two wavenumber intervals $508\text{--}528 \text{ cm}^{-1}$ and $803\text{--}823 \text{ cm}^{-1}$. We assume a surface emissivity of unity throughout the CO_2 band. While this may not be exactly true, our approach yields an effective surface temperature that correctly accounts for the surface emission across the CO_2 band. In addition, the method compensates to first order for neglecting the dust opacity.

3.2 Temperature inversion algorithm

The inversion of a temperature profile from planetary thermal emission is a typical “ill-posed” problem where arbitrarily small changes in the observed radiances lead to large differences in the inverted profile. Therefore, a classical inversion algorithm is too sensitive

to the measurement errors. It is however possible to retrieve a meaningful temperature profile with the regularization and stabilisation methods described by Craig and Brown (1986). These methods all introduce *a priori* informations on the solution. Here, we follow the specific algorithm designed by Conrath et al. (2000) for the inversion of the TES observations.

The radiative transfer equation is first linearized about a reference temperature profile \mathbf{T}_0 :

$$\Delta \mathbf{I} = \mathbf{K} \Delta \mathbf{T} \quad (1)$$

where \mathbf{K} is the derivative of the radiance with respect to the temperature profile. The differential quantities are $\Delta \mathbf{T} = \mathbf{T} - \mathbf{T}_0$, $\Delta \mathbf{I} = \mathbf{I} - \mathbf{I}_0$ where the radiance \mathbf{I}_0 is calculated for the initial temperature profile, \mathbf{I} is the measured radiance and \mathbf{T} the real temperature profile.

Then the inferred temperature profile minimizes the cost function

$$Q = (\Delta \mathbf{I} - \mathbf{K} \mathbf{F} \mathbf{a})^T \mathbf{E}^{-1} (\Delta \mathbf{I} - \mathbf{K} \mathbf{F} \mathbf{a}) + \gamma \mathbf{a}^T \mathbf{a} \quad (2)$$

where \mathbf{E} is the measurement error covariance matrix, \mathbf{F} a basis matrix, and \mathbf{a} the expansion of $\Delta \mathbf{T}$ on this basis ($\Delta \mathbf{T} = \mathbf{F} \mathbf{a}$). The solution of the problem is $\Delta \mathbf{T} = \mathbf{W} \Delta \mathbf{I}$ where

$$\mathbf{W} = \mathbf{S} \mathbf{K}^T (\mathbf{K} \mathbf{S} \mathbf{K}^T + \gamma \mathbf{E})^{-1} \quad (3)$$

with $\mathbf{S} = \mathbf{F} \mathbf{F}^T$. The actual nonlinearity of the problem is taken into account with three iterations of this procedure. Two parameters need to be adjusted, the matrix \mathbf{S} and the parameter γ . Following Conrath et al. (2000), we specify \mathbf{S} to be a smoothing gaussian function with a correlation length of 0.75 times the atmospheric scale height. The free parameter γ needs to be adjusted to the problem. Its value is chosen through numerical experiments. A value of γ that equalizes the traces of the matrix $\mathbf{K} \mathbf{S} \mathbf{K}^T$ and $\gamma \mathbf{E}$ is found to give the best compromise.

Using this technique, vertical temperature profiles can be retrieved from the surface up to a pressure level of 10 Pa (~ 35 km) with a vertical resolution of about one scale

height. The uncertainties on the retrieved temperatures are given by the covariance matrix \mathbf{WEW}^T . For a single PFS spectrum, they typically amount to ~ 2 K from 10 to 35 km, but increases in the first scale height above the surface to reach about ~ 5 K at the deepest pressure level.

Grassi et al. (2005) also performed a retrieval of the Martian temperature profiles from the PFS dataset. They used a similar method, although their cost function slightly differs from us. The comparison of the two retrieval methods are extremely satisfactory (Davide Grassi, personal communication). On a typical PFS session, the rms temperature difference amounts to 0.3 and 0.8K at 100 and 30 Pa respectively. Not surprisingly, the rms difference rises to 3K closer to the surface at 3 hPa.

3.3 Water column density retrieval

In the case of the water column density retrieval, given an assumption of its vertical profile, the number of parameters does not exceed the number of independent measurements. Therefore, the best-fit model is estimated through the usual χ^2 cost function across the 305–505 cm^{-1} interval. The solution for the best fit model is found with the Levenberg-Marquardt algorithm. We note that water lines grow stronger at wavenumbers shorter than 305 cm^{-1} , but so does the noise level in PFS spectra. Our analysis interval represents the best trade-off between strong line intensities and a low noise level.

The retrieved parameters are the water column density, and the surface emissivity at the following wavenumbers: 306.8, 320.0, 338.1, 358.3, 378.5, 390.6, 412.8, 431.0, 449.1, 467.3, 485.5, 503.7 cm^{-1} . These wavenumbers are chosen in-between the main H_2O signatures, well separated at our 1.3- cm^{-1} resolution. This approach implicitly assumes that the effective surface emissivity varies smoothly with wavenumber. This assumption was validated by the work of Smith et al. (2000) who separated the surface contribution from the atmospheric contribution on TES spectra. We note that Lellouch et al. (2000) retrieved a deep mineralogical (10% contrast) signature between 310 and 330 cm^{-1} from ISO/SW

spectra. However, such a deep feature would have been just obvious in TES and PFS/LW spectra, which are instead featureless in this wavenumber region (Fig. 2). Christensen et al. (2000) identify the strong, broad (50–100 cm^{-1}), features of hematite near 300, 450, and 525 cm^{-1} , but this mineral is present only on a small fraction of the martian surface. Our approach allows for an adequate fitting of the continuum emission over which the H_2O lines are formed. The surface temperature is taken, as explained above, as the mean of the brightness temperature in the two wavenumber intervals 508–528 cm^{-1} and 803–823 cm^{-1} . As explained above, this temperature may not strictly represent the actual surface temperature because of possible emissivity and dust effects in the 500–800 cm^{-1} range. Therefore, with this procedure we may not retrieve the correct surface emissivity at 20–35 μm , but we still estimate correctly the surface emission.

In contrast with the temperature retrievals, which are performed on each individual spectrum, the signal-to-noise ratio of a single PFS spectrum does not allow an accurate retrieval of the Martian water column abundance in the mean climatological conditions (10 pr- μm). Therefore, observations along one orbit are averaged with a sliding box of 9 consecutive spectra, and a sampling rate of every two spectra. For such an averaged spectrum, the NESR is never higher than $3 \times 10^{-8} \text{ W cm}^{-2} \text{ sr}^{-1}/\text{cm}^{-1}$ in the wavenumber range of interest. This NESR translates into an uncertainty of 1–2 pr- μm on the retrieved water column abundance. Figure 2 shows examples of fits of such PFS spectral averages in the regions of CO_2 and H_2O .

Other sources of errors are the uncertainties on the inverted atmospheric temperature, the effect of dust and water ice on the spectrum and the exact water vapor vertical distribution. The effect of temperature uncertainties is small (~ 1 pr- μm) as long as the atmosphere-surface temperature contrast is large (above 20K). The fact that we neglect aerosol opacity has also a marginal impact of the order of ~ 1 pr- μm . This stems for the fact that the dust optical thickness was low at 9 μm for most of the considered data set and that dust is even more transparent at 20–30 μm . As shown by Smith et al. (2000), the dust

and water ice contributions are weak and smooth at wavenumbers smaller than 600 cm^{-1} . Therefore our approach of fitting the continuum emission through surface emissivity takes into account most of the effect of the aerosol opacity. Our dataset is also limited to seasons where the dust content remains low on average. Regarding the water vertical distribution, our nominal values of the water column density are computed for a vertical profile uniformly mixed below the condensation level and equal to the saturated vapor pressure above this level, an approach similar to that of Smith (2002). However, we have also retrieved the water column density in a few cases for two extreme assumptions: a uniform H_2O mixing ratio up to the top of the atmosphere, and for a water column density confined to the first model layer ($\sim 3 \text{ km}$) above the surface. As expected given the low spectral resolution, spectral fits cannot distinguish between the various vertical profiles. As shown in Fig. 3 on the example of orbit 1023 ($L_s = 111^\circ$), these two extremes water vertical distributions yield column densities differing by typically $\pm 2 \text{ pr-}\mu\text{m}$ from the nominal model for all water columns below $30 \text{ pr-}\mu\text{m}$. The difference can reach $\sim 10 \text{ pr-}\mu\text{m}$ at larger water contents in the case where water is assumed to be confined in the first layer. In this case, the larger retrieved water column is related to the smaller thermal contrast between the surface and the water-containing atmospheric layer in a regime of strong line saturation¹.

Thus, with the exception of the Northern Polar maximum, we estimate that the quadratic combination of the above uncertainties leads to an uncertainty of the H_2O column abundance of $\pm 2\text{--}3 \text{ pr-}\mu\text{m}$.

Finally, as outlined by Smith (2002), the largest source of uncertainty lies in the value for the CO_2 -broadening parameter. Moreover it is a systematic uncertainty. The effect

¹We note here that an opposed behavior is observed for the water retrievals from PFS/SW at $2.56 \mu\text{m}$; in that case, confining the water to the first layer leads to *smaller* water columns, due to the general increase of absorption coefficients with temperature (see Ignatiev et al., in preparation). Assuming the water to be present *exclusively* in a near-surface layer therefore tends to reduce the disagreement between the PFS/LW and PFS/SW retrievals, but not enough for this to be a credible situation.

of increasing the CO₂-broadening parameter is to first order a linear decrease in the H₂O column abundance. As explained above (Sec. 3.1), we use the parameters calculated by Gamache et al. (1995). Given the uncertainties on the measured CO₂-broadening parameters (Gamache et al., 1995; Pollack et al., 1993), this gives a $\pm 25\%$ systematic error on the retrieved water column abundance. In particular, our H₂O linewidths are about 15% larger than assumed by Smith (2002) in his retrieval of the water column density from the TES observations (Smith used a constant scaling factor of 1.5 from the air-broadened values). For this reason, we retrieve a column density systematically 15% smaller than would have been retrieved by following Smith's (2002) approach.

Even though water ice is a key element of the water cycle (Montmessin et al., 2004), we did not attempt to retrieve water ice optical depth from the PFS database. Water ice is identified in the thermal range from its 825 cm⁻¹ absorption feature. Zasova et al. (2005) reported the detection of water ice clouds of several types from the PFS data, including orographic clouds, the equatorial cloud belt and the polar hood. However, we found that in many occasions, the shape of the PFS spectra shortward of 12.5 μm was not sufficiently reproducible and the S/N not sufficient to clearly disentangle the cloud signature from the broad dust absorption at 1075 cm⁻¹. This prevents a straightforward and systematic study of the water cloud cycle to be performed, similar to that achieved from TES (Pearl et al., 2001; Smith et al., 2001b; Smith, 2004).

4 Results on absolute abundances

4.1 Seasonal cycle

The seasonal distribution of the water vapor column density is shown in Fig. 4a, with a zoom on the Northern hemisphere in its summer season ($L_s = 90^\circ\text{--}180^\circ$) in Fig. 4b. The data, which cover the end of MY 26 and half of MY 27, are presented as a function of season and latitude by bins of 2° in L_s and 2° in latitude. Given the variation of the sampled local times with Martian season, this classical presentation assumes that seasonal variations of

water dominate over its diurnal variability (and implies that the Mars Express data are inappropriate to study diurnal variations of water). Although the temporal coverage is incomplete, some of the familiar trends of the water cycle are well recognized. The $L_s = 330^\circ\text{--}50^\circ$ range is characterized by low H_2O amounts (5–10 pr- μm), with a maximum at low Northern latitudes. This local maximum was previously best seen in the Viking/MAWD data (Jakosky and Farmer, 1982), and also reported from Mars Express/SPICAM (Fedorova et al., 2006). It may correspond to the extreme tail of the “tongue” of high water abundance developing equatorward since the previous year Northern summer peak, as best seen in the TES maps (Smith, 2002). The early Northern summer season ($L_s = 90^\circ\text{--}130^\circ$) is characterized by large latitudinal contrasts, with the water column decreasing monotonically from North to South from ~ 45 pr- μm poleward of 60° N to ~ 20 pr- μm at $40^\circ\text{--}55^\circ$ N and less than 10 pr- μm southward of 30° N. The progressive diffusion of water towards Northern mid-latitudes (corresponding to the initial formation of the “tongue”) is also seen, with e.g. the 20 pr- μm contour level shifting from 55° N at $L_s = 95^\circ$ to 40° N at $L_s = 120^\circ$. The Northern maximum abruptly stops at $L_s = 135^\circ$, with water vapor falling below 20 pr- μm everywhere on the planet. At $L_s = 150^\circ\text{--}180^\circ$, and although the spatial coverage is fairly incomplete, the PFS/LW data suggest a rather uniform water abundance over $0^\circ\text{--}60^\circ$ N at ~ 10 pr- μm , with little evidence for the low latitude ($0^\circ\text{--}30^\circ$ N) maximum observed by TES and SPICAM. In this respect, our results are more consistent with the behavior observed by MAWD. Data are very sparse after $L_s = 200^\circ$, due in particular to the instrumental problem mentioned above (Sec. 2.2).

4.2 Comparison with MGS/TES

While the water seasonal variation inferred from PFS/LW is qualitatively similar to findings from previous space missions, our results point to a substantially drier water cycle. In particular, the water amounts measured during the Northern summer never exceed 60 pr- μm . This contrasts to the peak column of 100 pr- μm reported by MGS/TES over the

North Pole at $L_s = 110^\circ\text{--}120^\circ$ for three consecutive Martian years (MY 24–26) (Smith, 2002, 2004) and the > 75 pr- μm observed by Viking/MAWD in 1978 (Jakosky and Farmer, 1982; Fedorova et al., 2004). The difference with TES is not restricted to the Northern Summer maximum. At $L_s = 0^\circ\text{--}50^\circ$, the mean water abundance inferred by PFS/LW over $0^\circ\text{--}30^\circ$ N is ~ 8 pr- μm , vs. ~ 12 pr- μm for TES. At $L_s = 150^\circ\text{--}180^\circ$ and $0^\circ\text{--}30^\circ$ N, the abundance is typically ~ 10 pr- μm for PFS/LW and $\sim 20\text{--}25$ pr- μm for TES.

The discrepancies between PFS/LW and TES are particularly significant since the two instruments utilize the same water features. One might, in principle, attribute them to actual temporal variability. However, Smith (2004) investigated temporal variability of atmospheric parameters (temperatures, water vapor column, ice and dust optical depths) in the TES dataset and found that year-to-year variability in the water vapor column remains usually at the < 5 pr- μm level, except near perihelion where variations of up to 10 pr- μm were observed over the South Pole maximum. (The South Pole Summer maximum is also the region where TES and MAWD show the largest differences, although Fedorova et al. (2004) argued that the MAWD estimates may be biased low due to dust opacity effects). These temporal variations might conceivably account for some of the differences between the TES and PFS/LW water values, but certainly not for the huge difference on the Northern Summer maximum.

In addition, TES performed systematic atmospheric measurements until 31 August 2004, providing water vapor measurements concomitant with Mars Express. These measurements, zonally-averaged and grouped by bins of 2° in L_s and 2° in latitude, are available in the form of a “TES climatology database”, kindly provided to us by M. Smith. Figure 5 (left panel) compares the water columns retrieved from PFS/LW and TES for all the (L_s , latitude) bins common to the two databases. Most of the measurements shown indicate low water amounts (< 20 pr- μm) characteristic of the season corresponding to the first-half of the year 2004 ($L_s \sim 330^\circ$ in MY 26 to $L_s \sim 80^\circ$ in MY 27). Figure 5 (left panel) clearly indicates that the TES values are typically 1.5 times larger than the PFS/LW values. Although

the TES and PFS measurements still do not pertain to the same regions (the longitude information is lost in Fig. 5), this is a strong indication of a systematic difference between the TES and PFS/LW measured values.

A possible physical reason would result from a diurnal variability of water vapor, as TES monotonically samples the 1 pm–3 pm time range, while the LT range covered by PFS varied linearly from LT = 3 pm at $L_s = 330^\circ$ to 8 am at $L_s = 60^\circ$ (see Fig. 1). A number of ground-based observations, particularly Sprague et al. (1996, 2001, 2006) and Hunten et al. (2000) have indicated that water abundances are generally highest at mid-day and lowest at dawn and dusk. However, the most recent and comprehensive dataset by Sprague et al. (2006), covering the 1998–1999 period, shows a variety of diurnal behaviors, with, in many occasions, a maximum in mid-morning (8 am–12 am) hours (see Fig. 11 of Sprague et al., 2006). The overall inconsistency of the results may reflect the difficulty to separate between diurnal and longitudinal (i.e. geographical) variations in these ground-based observations. From a reanalysis of the Mariner 9 data, Formisano et al. (2001) and Ignatiev et al. (2002) found a clear 12 am–2 pm peak of water in the Southern hemisphere at $L_s = 290^\circ$ – 310° , but they also observed the decrease and disappearance of this diurnal peak over $L_s = 330^\circ$ – 350° . Overall, the diurnal variability of water does not seem to be definitively established, and as mentioned previously, the PFS data are inadequate for this task.

We instead suggest here that the TES water columns are biased towards high values. A careful re-examination of the TES retrievals by M. Smith (priv. comm., and to be published elsewhere) gives credit to this hypothesis. In brief, Smith’s reanalysis is the following: the TES retrievals were based on measurements at either 6.25 and 12.5 cm^{-1} resolution, and made use of water signatures at 250, 280, 300 and 330 cm^{-1} . With the exception of the period extending from MY 25, $L_s = 90^\circ$ (December 2000) to MY 26, $L_s = 120^\circ$ (January 2003), most of the data were taken in the 12.5- cm^{-1} mode. At 6.25 cm^{-1} resolution, the four bands give very consistent results. However, at 12.5 cm^{-1} resolution, the measurements in the 300 and 330 cm^{-1} bands give a much higher water abundance than the 250 and

280 cm^{-1} bands. When the 300 and 330 cm^{-1} bands are ignored, the abundance inferred from the 12.5 cm^{-1} resolution data is lower by about 30% than when they are included, and a better repeatability between the three Martian years is achieved.

In fact, a fraction of the inter-annual variability shown in Fig. 12 of Smith (2004) may be attributed to the change of observing mode. The comparison between TES and PFS/LW in the left panel of Fig. 5 is entirely based on 12.5 cm^{-1} TES measurements, which according to the previous arguments, should be decreased by $\sim 30\%$. In addition, we believe that the TES values should be further decreased by 15% due to the choice of the $\text{H}_2\text{O-CO}_2$ collisional linewidths. The right panel of Fig. 5 shows the comparison between PFS/LW and TES after making these corrections. In this panel, rather than applying uniformly the 30% correction, we in fact use a new version of the TES climatology database, prepared by M. Smith, and in which the “12.5- cm^{-1} problem” was fixed, and we further apply the 15% correction. Clearly, the agreement between PFS/LW and these “corrected” TES values is now satisfactory.

4.3 Comparison with Mars Express/SPICAM and OMEGA

A systematic comparison of our results with those from the other two Mars Express instruments, SPICAM (Fedorova et al., 2006) and OMEGA (Encrenaz et al., 2005b; Melchiorri et al., 2006), will await the availability of databases such as the TES one. For the time being, we note that there is a general agreement between the three instruments that the water Northern summer maximum does not exceed 60 $\text{pr-}\mu\text{m}$. On the other hand, measurements from SPICAM in the 1.38 μm band tend to indicate an even drier water cycle than we infer. For example, the mean low-latitude abundance at $L_s = 0^\circ\text{--}50^\circ$ inferred from SPICAM is ~ 5 $\text{pr-}\mu\text{m}$, vs ~ 8 $\text{pr-}\mu\text{m}$ for PFS/LW. The same numbers hold for the equatorial abundance during the Northern Summer maximum season ($L_s = 90^\circ\text{--}140^\circ$). Fedorova et al. (2006) noted that the SPICAM values are generally low compared to most other results. Regarding the comparison with OMEGA, while we get a similar value for the Northern

Summer high-latitude maximum, we measure somewhat less water at mid-Northern latitudes, e.g. $\sim 15\text{--}18$ pr- μm at 40° N for $L_s = 95^\circ\text{--}110^\circ$, vs. $\sim 20\text{--}25$ pr- μm for OMEGA (Encrenaz et al., 2005b). Similarly, OMEGA measurements (Melchiorri et al., 2006) give more water in the $L_s = 330^\circ\text{--}40^\circ$ period ($10\text{--}15$ pr- μm at $0^\circ\text{--}30^\circ$ N, generally consistent with TES and MAWD) than PFS/LW.

Our water vapor amounts are thus generally intermediate between those from SPICAM and OMEGA. However, we note that the water determinations from OMEGA and SPICAM are subject to a number of complications (i) the $1.38\ \mu\text{m}$ band used by SPICAM (and previously by MAWD) and the $2.56\ \mu\text{m}$ band used by OMEGA are affected by dust scattering. So far, the published SPICAM (and OMEGA) data were analyzed with no account for dust. This may lead to an underestimate of the water columns, although Fedorova et al. (2006) report that the effect is negligible for total airmasses lower than 3 (ii) the spectral resolution of SPICAM ($3.5\ \text{cm}^{-1}$) is not high enough for the true (100% transmission) continuum to be reached in-between the spectral features due to water. Thus the retrieval procedure consists of an iterative process to determine both the water abundance and the surface albedo. To mimick the likely behavior of surface ices/minerals, the surface albedo is constrained to vary smoothly (i.e. convolved to a $12\text{--}20\ \text{nm}$ resolution). Results on water are sensitive to the precise smoothing value (at the 5–15% level, A. Fedorova, priv. comm.) (iii) stray light is present in the SPICAM data at the $> 10\%$ level, causing the CO_2 and H_2O bands to be shallower than they would be in the absence of scattered light. This may cause an underestimate of the H_2O abundances by as much as 40% in average (Fedorova et al., 2006). In fact, it should be noted that the SPICAM data give 1.7 times less water than was inferred from the reanalysis of the MAWD data by Fedorova et al. (2004) (iv) at the resolution of the OMEGA measurements ($\lambda/\Delta\lambda \sim 130$ in the relevant spectral range), the H_2O band appears as a 1–6% deep feature covering only a few spectral elements. This requires a perfect correction of the instrumental transfer function, achieved through ratio of spectra by a “reference spectrum” taken over Olympus Mons. The uncer-

tainty in the OMEGA water determinations include S/N limitations ($< 30\%$ in the water column), and uncertainties, estimated to ± 2 pr- μm , in the amount of water present in the reference spectrum. A further uncertainty, difficult to quantify, is associated to the hypothesis of perfect cancellation of mineralogic features between the analyzed spectra and the reference spectrum. None of the above complications is present in the water retrievals from PFS/LW, which we believe are therefore more trustworthy, although, as mentioned above, the PFS/LW values are very sensitive to the value of the H_2O - CO_2 collisional linewidths (in fact more than the OMEGA and SPICAM values, as the 1.38 and 2.56 μm bands are less saturated than the rotational lines). We also note that a number of the above effects, especially those affecting the OMEGA retrievals, are more serious at low band depths, which might explain that the relative agreement between the three instruments is better at high water contents than at columns < 15 pr- μm , although a complete study is needed.

4.4 Comparison with other and ground-based measurements

Besides the MGS and Mars Express results, numerous other measurements of Martian water vapor are available, including a number of more or less disparate Earth-based or spaceborne observations, and the more extensive ground-based database built over the years by the University of Arizona group from observations at 0.82 μm (Sprague et al., 1996, 2001, 2003, 2006, and references therein). Although comparisons are less straightforward, especially given the huge differences in spatial resolution, we believe that the ensemble of data tends to give support to our conclusion that the atmosphere as a whole is drier than indicated by the initial MGS/TES results (Smith, 2002). Here we make comparisons with only some of the most recent (< 10 years) results. For the year 1999 (MY 24), Sprague et al. (2006) report a Northern maximum of ~ 60 pr- μm at $L_s = 90^\circ$ – 115° , with higher individual values being exceptionally rare. As shown in the same paper, and initially noted by Smith (2002), the latitudinal distribution reported by TES for a 5-day average around June 1, 1999 ($L_s = 147^\circ$) is 1.5 times wetter than in the ground-based measurements of Sprague et

al. on this date. For the same season ($L_s = 150^\circ\text{--}160^\circ$) but during the previous Martian year (in July-August 1997), Burdgorf et al. (2000) report ISO IR measurements a disk-average (i.e. sampling the low latitudes) abundance of 12 ± 3.5 pr- μm . This is intermediate between the ~ 10 pr- μm typical of the $30^\circ\text{ S--}30^\circ\text{ N}$ latitudes in the PFS/LW spectra, and the globally-averaged value of 15 pr- μm inferred from TES at this period (Fig. 9 of Smith, 2004). For the same epoch, an even lower value of 6 ± 4 pr- μm at 19° N was obtained from Pathfinder observations at sunrise and sunset (Titov et al., 1999). A few other disk-resolved measurements are available from ground-based IR observations. At $L_s = 67^\circ$ in MY 23, Novak et al. (2002) determined a maximum of 24 pr- μm at $60\text{--}75^\circ\text{ N}$ from ground-based HDO observations. At $L_s = 206^\circ$ in MY 26 (June 2003), Encrenaz et al. (2005a) report a maximum of 17 ± 9 pr- μm at $20^\circ\text{ S--}20^\circ\text{ N}$. While we do not have values from PFS/LW for these two values of L_s , the TES values corresponding to these conditions are ~ 30 and ~ 20 pr- μm , respectively. Finally, spaceborne submillimeter observations by SWAS and ODIN indicate global abundances of 12 ± 6 pr- μm for $L_s = 166^\circ\text{--}233^\circ$ in 2001 (dust storm, MY 25) (Gurwell et al., 2005), and 13 ± 3 pr- μm at $L_s = 204^\circ$ and 10 ± 2 pr- μm at $L_s = 294^\circ$ in 2003 (MY 26) (Biver et al., 2005). A mean value of ~ 12 pr- μm over $L_s = 165^\circ\text{--}200^\circ$ agrees very well with our map and with the globally-averaged inferred from TES for MY 25, but is somewhat below the mean ~ 16 pr- μm value for MY 24 (see Fig. 9 of Smith, 2004). This is probably an effect of the change of observing mode in the TES data, as discussed above.

5 Results on specific behaviors and comparisons with LMD/GCM simulations

5.1 Geographical distribution

5.1.1 Low-latitudes

Figure 6 shows water column maps as a function of latitude and longitude. In these maps, the retrieved water columns are scaled to a common 610 Pa pressure (i.e. divided by $P_{surf} / 610$, where P_{surf} is the average pressure over the nine consecutive spectra used to retrieve water) to remove topographic effects, and then averaged by 2° latitude, 4° longitude bins, producing a geographical map of water vapor, which can be compared to similar presentations by Smith (2002, 2004) and Fedorova et al. (2006). In the first panel of Fig. 6, where all of our data are included, weak local maxima can be distinguished at 0° – 60° E and 60° – 140° W in the inter-tropical region, although they appear subdued in comparison with the high-latitude maximum. These maxima, which correspond to the regions of Arabia and Tharsis, were also clearly seen in the TES data (see plate 3 of Smith (2002)). The other panels in Fig. 6 show the geographical distribution for three separate bins in L_s , with a color scale matched to the mid-latitude abundances. The Arabia and Tharsis maxima are well visible at $L_s = 330^\circ$ – 60° and especially at 155° – 210° , with an enhancement of a factor ~ 2 compared to other longitudes. The Arabia maximum is also visible in the unscaled water columns (not shown). At $L_s = 90^\circ$ – 150° , the lack of data at 15° – 50° E longitudes makes it impossible to identify the Arabia maximum, while the Tharsis maximum is less marked than at other seasons. Caution should be exercised before claiming a “seasonal” variability of the Arabia and Tharsis maxima, due to the variability of the sampled local times with L_s , and the maximum longitudinal contrast found at $L_s = 155^\circ$ – 210° may in fact reflect a contrast enhancement at mid-morning hours (8.30–12 am). Still, we note that the maps presented by Smith (2004) at $L_s = 105^\circ$ – 125° for MY 24–26 also suggest that the geographical distribution of water vapor at that season is significantly different from other

seasons.

As noted by Smith (2002), water columns, scaled to a fixed pressure, show at low-to-mid latitudes a positive correlation with albedo, and an anticorrelation with thermal inertia. The correlation with albedo was also noted by Jakosky and Farmer (1982) from Viking/MAWD data and by Rosenqvist et al. (1992) from Phobos/ISM observations. As Tharsis and Arabia are also regions of high topography, the maxima found there on an annual basis may suggest an anticorrelation with surface pressure. More direct evidence for such an anticorrelation is shown below. Although all three parameters may have a direct or indirect influence on the atmospheric water amounts, through surface temperature control and atmosphere-regolith exchanges, general climate models are needed to identify the cause of the uneven geographical distribution of low-latitude atmospheric water and its possible seasonal/diurnal variability.

To help interpret our water vapor observations, we performed some comparisons with the Global Climate Model (GCM) developed at the Laboratoire de Météorologie Dynamique (Forget et al., 1999) which is able to simulate the atmospheric water cycle (Montmessin et al., 2004) by taking into account the exchanges between surface ice and the atmosphere as well as the transport and turbulent mixing of water, relying on simplified microphysics for cloud formation. It provides distributions of H₂O vapor (and clouds) in good agreement with MGS TES observations (Montmessin et al., 2004), and thus predict amounts of water vapor usually higher than our retrievals. A detailed comparison would be out of scope of this paper. Nevertheless we used the model to help interpret the longitudinal distributions observed in Fig. 6.

Figure 7 (left panel) shows a water column map predicted by the GCM for the season $L_s = 180^\circ - 210^\circ$ (scaled to the 610-Pa pressure level). This is a season when spatial variations in the tropics are well observed in the PFS data, as shown in Fig. 6 (bottom right). The simulation produces spatial variations with maxima of water vapor near Tharsis (120° W) and Arabia Terra (30° E) in qualitative agreement with the observations. This sug-

gests that these spatial variations are probably caused by some atmospheric dynamical or physical processes, and that a subsurface water source (not included in the model) is not necessarily involved. What is the origin of the modeled spatial variations? Figure 7 (right panel) shows the horizontal wind streamlines at 3 km above the surface (a good altitude to illustrate the transport in the lower atmosphere) superimposed on the water vapor map. One can see that the water vapor spatial distribution is, to first order, controlled by the oscillation of the atmospheric flow. For instance the minimum of water vapor around (30° S, 50° W) clearly results from a flow of dry air originating from the mid-southern latitudes, and that the maximum near (10° S, 30° E) is due to a convergence of relatively wet air in this area.

We note however that the relative variations seem to be significantly weaker in the model than in the observations, although this situation does not hold at every altitude. Figure 8 (left panel) shows a longitude-altitude cross section of the daytime atmospheric vapor and ice mixing ratios at 0° N latitude. These plots show that the modeled water vapor is not completely vertically mixed, even below the saturation level. The concentration of water vapor is maximum between about 10 and 22 km (above Mars zero datum), probably because of the sublimation of the cloud particles above. The horizontal variations within this relatively "wet layer" are significantly larger than for the total column, as shown in Fig. 8 (right panel). A comparison of Fig. 8 and Fig. 6 reveals that the patterns in the simulated water vapor at 20 km better match the magnitude of the contrast in the water vapor column map retrieved with PFS. There again, the observed spatial variations can be explained by the modulation (stationary wave) of the atmospheric flow induced by the surface properties (topography and/or albedo of the surface) and a convergence of air near (20° S, 30° E) (Fig. 8, right). These mid-atmosphere variations could contribute to the apparent water column variations detected by PFS. However, our analysis in Sec. 3.3 shows that PFS/LW spectra are just marginally sensitive to the water vertical distribution. In addition, the maxima predicted by the GCM at 20 km are rather present in the Southern

hemisphere. The origin of the differences in the relative geographical variations between datasets and models thus remains to be explored in greater details.

5.1.2 High Northern latitudes

As mentioned above, the highly-inclined Mars Express orbit provided good visibility of the high latitudes, allowing in principle to study the behavior of water vapor at sublimation onset. In the PFS data, however, the need to average several spectra to build a sufficient S/N, and the fact that a few spectra are usually unusable at the beginning of each orbit, limit the measurements very close to the pole, so that the maps we present do not, in general, extend much beyond 80° N. (Unfortunately, SPICAM is also limited in this respect due to the difficulty of correcting for dust effects at high emission and solar zenith angles (Fedorova et al., 2006) while the OMEGA water measurements at $2.56 \mu\text{m}$ are compromised over the polar regions by the mixing of the water band with the signature of small icy grains (Melchiorri et al., 2006)). A few exceptions occur near $L_s = 68^\circ\text{--}75^\circ$, where the water latitudinal profile is available up to the North pole. As shown in Fig. 9, at $L_s = 69^\circ$, (orbit 685), water exhibits a narrow bulge between 72° N and 83° N, where the scaled water columns are ~ 3 times larger than at lower and higher latitudes. This behavior is consistent with the mechanisms proposed for the return of water to the permanent cap during spring (e.g. Bass and Paige, 2000; Richardson and Wilson, 2002; Montmessin et al., 2004). Water ice accumulated at mid-to-high latitudes during the previous seasons sublimates, is "vacuum-transported" along with the retreating CO_2 seasonal cap, and redeposited as frost between the cap edge and the pole. The low water vapor observed northward of 83° N is associated with low surface temperatures (~ 155 K) at 80° N and beyond, characteristic of CO_2 ice. The correlation of Viking IRTM and MAWD measurements (Bass and Paige 2000) clearly indicates that the water amounts remain low whenever the surface temperature is below ~ 160 K.

5.2 Vertical distribution

As mentioned in Sec. 2.1, the spectral resolution of PFS/LW does not allow a direct retrieval of the water vertical profile, and the combination of PFS/LW and PFS/SW observations also did not appear to be fruitful so far. Information on the vertical profile of water, or more precisely, on the extent to which it is well mixed in the atmosphere, can still be obtained by investigating the correlation of the retrieved columns with topography.

5.2.1 Behavior near large volcanos

In Fig. 10, we show water retrievals for three orbits (37, 925, 370) crossing areas of large topographic contrast (Olympus at 19° N, 227° E, Elyseum at 23° N, 147° E, and Ascræus at 11° N, 104° W). The topographic signature of the large volcanos is well visible on the absolute (unscaled) water columns (top panels of Fig. 10). The behavior of the water volume mixing ratio below the saturation level is somewhat less clear. As shown in the bottom panels of Fig. 10 — in which the thin lines indicate topography — although error bars are large, there is a suggestion for a $\sim 80\%$ increase of the water mixing ratio in the Southern flank of Olympus Mons, while on Elyseum results are consistent with a $\sim 100\%$ increase on the Northern flank. On Ascræus Mons, there is evidence for a comparable decrease of the water abundance over the top of the volcano. The altitude of water vapor saturation over the volcanos is always higher than one scale height (~ 10 km) with respect to the local topography. However, we note that our determination of the saturation altitude is rather uncertain as the inversion of the temperature profile from the CO_2 band above the volcanos is particularly affected by contamination from surface thermal emission. Overall, our results do not give a consistent picture for the various volcanos but indicate, at most, moderate variations of the water mixing ratio in the vicinity of the large volcanos. This result contradicts previous findings from Phobos-2/ISM observations, which indicated a factor-of-five increase in water above the volcanos and was interpreted as due to atmosphere-regolith

exchanges with intense day time desorption of water from the volcanic regolith (Titov et al., 1994). We also note that moderate ($\pm 50\%$) variations of the surface water mixing ratio over the volcanos are predicted in the European Martian Climate Database, although such variations might conceivably be somewhat subdued at the low spatial resolution (e.g. 3.75° longitude) of the database. This database is based on general circulation models coupled with chemistry (Forget et al., 1999; Montmessin et al., 2004) in which atmosphere-subsurface exchanges are ignored.

5.2.2 Correlation with pressure

Figure 11 presents the water columns (absolute and normalized to 610 Pa) as a function of pressure for the individual retrievals. To avoid large seasonal effects, and in particular the high water contents characteristic of Northern summer at high latitudes, we consider here only measurements at latitudes between -30° and $+30^\circ$, most of which indicate water columns in the range 4–18 pr- μm . In addition, only measurements with relative uncertainties of less than 20% (typically $< 1\text{--}4$ pr- μm) are included. Figure 11 presents the results for all orbits together (top panels), as well as for two seasons separately, around Northern Spring equinox ($L_s = 330^\circ\text{--}60^\circ$), and Northern Summer and early fall ($L_s = 90^\circ\text{--}200^\circ$) respectively. Figure 11 indicates that, as expected for a generally well-mixed water distribution, the absolute water columns are positively correlated with pressure. However, as can be seen, particularly when the two seasons are shown separately, the absolute water columns increase more slowly than they would for a linear dependence, so that the normalized water appears to be anticorrelated with pressure. To assess the statistical significance of this result, we calculated in each case, the Spearman (rank order) correlation coefficient, and the number of standard deviations (z_d) at which D, the sum-squared difference of ranks, deviates from its null hypothesis expected value. As indicated in Table 1, the results are highly significant in all cases. Our results thus indicate that water is not completely well-mixed,

and that dividing by $P_{surf} / 610$ actually overcompensates for topography. For the two seasons separately, Table 1 also gives the results of a linear fit to the data points in Fig. 11, in the form $\text{H}_2\text{O}(\text{pr-}\mu\text{m}) = a + b \times P_{surf} \text{ (Pa)}$, both in the case of absolute and normalized water. The b coefficients have comparable magnitudes and opposite signs for the two cases. This points to a situation intermediate between full mixing and confinement of water in a surface layer. This behavior, which holds for the two seasons, is in fact not consistent with a water profile defined by uniform mixing and saturation level independent of the surface pressure : such a situation would lead to a decrease of the mean mixing ratio with decreasing surface pressure, i.e. to a *positive* correlation between scaled water and surface pressure.

Direct measurements on the vertical distribution of water are limited. In the absence so far of adequate instrumentation on descent probes, alternate means to vertically resolve the water profile include (i) occultation and limb measurements (ii) absorption measurements with multiple paths in a given atmospheric column (iii) spectrally-resolved line spectroscopy. From solar occultation measurements with Phobos 2/Auguste obtained at $L_s = 2^\circ\text{--}18^\circ$, Rodin et al. (1997) observed an approximately uniform H_2O mixing ratio over 10–25 km, and a sharp decrease above. Davies (1979) used multiple-angle observations of the Viking 1 lander from Viking 1/MAWD to infer a uniform distribution of water below 10 km above the lander site at $L_s = 102^\circ$. From a similar technique but observing the Sun from the Martian surface, Titov et al. (1999) found instead that water is confined in the first 1–3 kilometers at $L_s = 150^\circ$. The variations of the residence altitude and condensation level of water with season were more completely established from disk-averaged mm-wave spectroscopy by Clancy et al. (1996), who found that water is confined to altitudes below 10 km near aphelion ($L_s = 71^\circ$), but invades the entire atmosphere up to 50–70 km near perihelion ($L_s = 251^\circ$). Complementary observations by Encrenaz et al. (1991, 1995), Gurwell et al. (2000) and Biver et al. (2005) support this picture, as well as numerical simulations (Richardson and Wilson, 2002; Montmessin et al., 2004). Titov (2002) reviewed most of

these observations and also concluded to a seasonal variation of the thickness of the well-mixed layer, from only ~ 5 km at $L_s = 90^\circ$ – 150° to ~ 20 – 25 km at $L_s = 330^\circ$ – 30° .

Our results on the correlation of water with surface pressure tend to agree with those from TES. Smith (2002) reported that a linear rescaling of the water column to a fixed pressure is a slight overcompensation for topography. He further found that the anticorrelation of scaled water with surface pressure is stronger in the Northern hemisphere than in the Southern, i.e., that on an annually-averaged basis water is more fully mixed in the South than in the North. Smith (2002) interpreted this result in the framework of the above picture of the time-varying hygropause, since water abundances are large in the South near perihelion and large in the North near aphelion.

We have further explored whether this anti-correlation is simulated by the LMD/GCM. Figure 12 shows the GCM-predicted water columns normalized to 610 Pa as a function of pressure for time and location corresponding to each PFS spectrum used in Fig. 11, bottom right panel ($L_s = 90^\circ$ – 200° in the tropics, 30° S– 30° N). As mentioned above, the modeled water vapor columns are somewhat higher than in the PFS observations (the model was calibrated with TES). Spatial variations are predicted, but there is no correlation with surface pressure. This fundamental difference suggests that a key process controlling the water vapor distribution is missed by the model. In particular, the model takes into account the dynamical and saturation processes that could lead to a dependence of the water mixing ratio or the saturation altitude with the surface properties, but it does not include a subsurface source.

Moreover, the observed anti-correlation between scaled water and surface pressure points to the fact that a small amount of “background” water (typically 3–4 pr- μm , as indicated by the a coefficients in Table 1) may be present independently of altitude (except on the top of volcanos), presumably due to regolith-atmosphere exchanges. We also note that as indicated by the a , b coefficients in Table 1 (and specifically by the a/b ratios), the relative importance of the well-mixed and regolith-exchange-dominated water components do not

appear to show strong variations between the two seasons we investigated. Böttger *et al.* (2005) have studied the effect of regolith-atmosphere exchanges on the martian water cycle within the frame of a general circulation model. They found that, at 23° N, 10% of the total column density could exchange between the regolith and the atmosphere during a diurnal cycle. This represents 1-2 pr- μm , smaller, but comparable to the 3-4 pr- μm suggested by our observations.

6 Summary

We have analyzed the Mars Express PFS/LW observations of Mars acquired over 2004–2005 in terms of the seasonal, geographical and vertical distribution of water in the Martian atmosphere. The main results are as follows:

1. The seasonal (L_s , latitude) behavior of water is generally consistent with previous findings from Viking/MAWD and MGS/TES and concomitant observations from Mars Express/SPICAM, but the absolute amounts we infer are lower and higher than the values from TES and SPICAM respectively, by factors of about 1.5. The maximum water columns measured at high Northern latitudes in summer are ~ 60 pr- μm . Causes for the disagreement with TES have been identified. As our dataset is clearly inferior in completeness to the TES database, we believe modellers should continue to regard the TES database as the reference, but after a downward revision of the abundances is performed.
2. The geographical distribution of water shows two local maxima at low latitudes, corresponding to the regions of Tharsis and Arabia, where water columns scaled to a common pressure are enhanced by a factor of ~ 2 (with possible seasonal or diurnal variability) with respect to other longitudes. This confirms previous results from TES. LMD/GCM simulations suggest

that this geographical distribution is controlled by atmospheric dynamics.

3. Within factor-of-two error bars, the mean water mixing ratio above large volcanos is found to be the same as in surrounding regions. This contradicts early findings from Phobos 2/ISM.
4. During the retreat of the seasonal polar cap in the northern spring, we observe a bulge in water column centred at the seasonal cap edge. This behavior is consistent with the mechanism proposed for the return of water from the seasonal polar cap to the permanent polar cap.
5. While, as expected, the water columns are positively correlated with surface pressure, the data also indicate that the normalized (i.e. scaled to a fixed pressure) are anti-correlated with pressure, indicating an intermediate situation between the state where water is controlled by atmospheric saturation and the case of confinement in a surface layer, and pointing to a significant role of regolith-atmosphere exchange.

Acknowledgments

We sincerely thank Michael Smith who kindly distributed the TES/MGS climatology database, and made us available a revised version of the TES/MGS water retrieval ahead of publication.

References

- Barker, E.S. 1976. Martian atmospheric water vapor observations: 1972-74 apparition. *Icarus* 28, 247–268.
- Barker, E.S., Schorn, R.A., Woszczyk, A., Tull, R.G., Little, S.J., 1970. Mars: Detection of atmospheric water vapor during the southern hemisphere spring and summer season. *Science* 170, 1308–1310.
- Bass, D.S., Paige, D.A., 2000. Variability of Mars' North Polar Water Ice Cap. II. Analysis of Viking IRTM and MAWD. *Icarus* 144, 397-409.
- Biver, N., and 10 colleagues 2005. Wide-band observations of the 557 GHz water line in Mars with Odin. *Astron. Astrophys.* 435, 765-772.
- Böttger, H. M., Lewis, S. R., Read, P. L., Forget, F. 2005. The effects of the martian regolith on GCM water cycle simulations. *Icarus* 177, 174-189.
- Burgdorf, M.J., and 11 colleagues 2000. ISO Observations of Mars: An Estimate of the Water Vapor Vertical Distribution and the Surface Emissivity. *Icarus* 145, 79-90.
- Clancy, R.T., Grossman, A.W., Muhleman, D.O., 1992. Mapping Mars water vapor with the Very Large Array. *Icarus* 100, 48-59.
- Clancy, R.T., Grossman, A.W., Wolff, M.J., James, P.B., Rudy, D.J., Billawala, Y.N., Sandor, B.J., Lee, S.W., Muhleman, D.O., 1996. Water vapor saturation at low altitudes around Mars aphelion: A key to Mars climate?. *Icarus* 122, 36-62.
- Conrath, B., Curran, R., Hanel, R., Kunde, V., Maguire, W., Pearl, J., Pirraglia, J., Welker, J., 1973. Atmospheric and surface properties of Mars obtained by infrared spectroscopy on Mariner 9. *J. Geophys. Res.* 78, 4267-4278.
- Conrath, B.J., J.C. Pearl, M.D. Smith, W.C. Maguire, P.R. Christensen, S. Dason, and M.S., Kaelberer 2000. Mars Global Surveyor Thermal Emission Spectrometer (TES) observations: Atmospheric temperatures during aerobraking and science phasing. *J. Geophys. Res.* 105, 9509–9520.

- Craig, I. J. D., and J. C. Brown 1986. *Inverse problems in astronomy*. Adam Hilger, Bristol, UK.
- Christensen, P. R., and 15 colleagues 2000. Detection of crystalline hematite mineralization on Mars by the Thermal Emission Spectrometer: Evidence for near-surface water. *J. of Geophys. Res.* 105, 9623-9642.
- Encrenaz, T., Lellouch, E., Rosenqvist, J., Drossart, P., Combes, M., Billebaud, F., de Pater, I., Gulkis, S., Maillard, J.P., Paubert, G., 1991. The atmospheric composition of Mars - ISM and ground-based observational data. *Ann. Geophys.* 9, 797-803.
- Encrenaz, T., Lellouch, E., Cernicharo, J., Paubert, G., Gulkis, S., 1995. A tentative detection of the 183-GHz water vapor line in the Martian atmosphere: Constraints upon the H₂O abundance and vertical distribution. *Icarus* 113, 110-118.
- Encrenaz, T., and 10 colleagues 2005a. Infrared imaging spectroscopy of Mars: H₂O mapping and determination of CO₂ isotopic ratios. *Icarus* 179, 43-54.
- Encrenaz, T., and 10 colleagues 2005b. A mapping of Martian water sublimation during early northern summer using OMEGA/Mars Express. *Astron. Astrophys.* 441, L9-L12.
- Farmer, C.B., Davies, D.W., Holland, A.L., Laporte, D.D., Doms, P.E., 1977. Mars: Water vapor observations from the Viking orbiters. *J. Geophys. Res.* 82, 4225-4248.
- Fedorova, A.A., Rodin, A.V., Baklanova, I.V., 2004. MAWD observations revisited: seasonal behavior of water vapor in the Martian atmosphere. *Icarus* 171, 54-67.
- Fedorova, A., Korablev, O., Bertaux, J.-L., Rodin, A., Kiselev, A., Perrier, S., 2006. Mars water vapor abundance from SPICAM IR spectrometer: Seasonal and geographic distributions. *J. Geophys. Res.* 111. doi:10.1029/2006JE002695.
- Forget, F., Hourdin, F., Fournier, R., Hourdin, C., Talagrand, O., Collins, M., Lewis, S.R., Read, P.L., Huot, J.-P., 1999. Improved general circulation models of the Martian atmosphere from the surface to above 80 km. *J. Geophys. Res.* 104, 24155-24176.
- Forget, F., and 12 colleagues 2006. The new Mars climate database. Second International Workshop on Mars Atmosphere Modelling and Observations. Granada, Spain.

- Formisano, V., Grassi, D., Ignatiev, N.I., Zasova, L., 2001. IRIS Mariner 9 data revisited: water and dust daily cycles. *Planet. Space Sci.* 49, 1331-1346.
- Formisano, V., Grassi, D., Ignatiev, N., Zasova, L., Maturilli, A., 2002. PFS for Mars Express: A new approach to study Martian atmosphere. *Adv. Space Res.* 29, 131-142.
- Formisano, V., and 46 colleagues 2005. The Planetary Fourier Spectrometer (PFS) onboard the European Mars Express mission. *Planet. Space Sci.* 53, 963-974.
- Gamache, R. R., S.P. Neshyba, J.J. Plateaux, A. Barbe, L. Régalia, and J. B. Pollack 1995., CO₂-broadening of water-vapor lines. *J. Mol. Spectrosc.* 170, 131–151.
- Giuranna, M., and 19 colleagues 2005. Calibration of the Planetary Fourier Spectrometer long wavelength channel. *Planet. Space Sci.* 53, 993-1007.
- Grassi, D., Ignatiev, N.I., Zasova, L.V., Maturilli, A., Formisano, V., Bianchini, G.A., Giuranna, M., 2005. Methods for the analysis of data from the Planetary Fourier Spectrometer on the Mars Express Mission. *Planet. Space Sci.* 53, 1017-1034.
- Gurwell, M.A., and 20 colleagues 2000. Submillimeter Wave Astronomy Satellite Observations of the Martian Atmosphere: Temperature and Vertical Distribution of Water Vapor. *Astrophys. J.* 539, L143-L146.
- Gurwell, M.A., Bergin, E.A., Melnick, G.J., Tolls, V., 2005. Mars surface and atmospheric temperature during the 2001 global dust storm. *Icarus* 175, 23-31.
- Hourdin, F., Le van, P., Forget, F., Talagrand, O. 1993. Meteorological variability and the annual surface pressure cycle on Mars. *J. Atmos. Sci.* 50, 3625-3640.
- Hunten, D.M., Sprague, A.L., Doose, L.R., 2000. Correction for Dust Opacity of Martian Atmospheric Water Vapor Abundances. *Icarus* 147, 42-48.
- Ignatiev, N.I., Zasova, L.V., Formisano, V., Grassi, D., Maturilli, A., 2002. Water vapour abundance in Martian atmosphere from revised Mariner 9 IRIS data. *Adv. Space Res.* 29, 157-162.
- Jacquinet-Husson, N., E. Arié, J. Ballard, G. Bjoraker, B. Bonnet, L. R. Brown, C. Camy-Peyret, J.-P. Champion, A. Chédin, A. Chursin, C. Clerbaux, G. Duxbury, J.-M. Flaud,

- N. Fourrié, A. Fayt, G. Graner, R. Gamache, A. Goldman, V. Golovko, G. Guelachvili, J.-M. Hartmann, J.-C. Hilico, J. Hillman, G. Lefèvre, E. Lellouch, S. N. Mikhaïlenko, O. V. Naumenko, V. Nemtchinov, D. A. Newnham, A. Nikitin, J. Orphal, A. Perrin, D. C. Reuter, C. P. Rinsland, L. Rosenmann, L. S. Rothman, N. A. Scott, J. Selby, L. N. Sinitza, J. M. Sirota, A. M. Smith, K. M. Smith, V. G. Tyuterev, R. H. Tipping, S. Urban, P. Varanasi, and M. Weber 1999. The 1997 spectroscopic GEISA databank. *J. Quant. Spectrosc. Rad. Transfer* 62, 205–254.
- Jakosky, B.M. 1985. The seasonal cycle of water on Mars. *Space Sci. Rev.* 41, 131-200.
- Jakosky, B.M., Farmer, C.B., 1982. The seasonal and global behavior of water vapor in the Mars atmosphere - Complete global results of the Viking atmospheric water detector experiment. *J. Geophys. Res.* 87, 2999-3019.
- Jakosky, B.M., Haberle, R.M., 1992. The seasonal behavior of water on Mars. In: Kieffer, H.H., Jakosky, B.M., Snyder, C.W., Matthews, M.S. (Eds.), *Mars*. University of Arizona Press, Tucson, pp. 969-1016.
- Lellouch, E., Encrenaz, T., de Graauw, T., Erard, S., Morris P., Crovisier, J., Feuchtgruber, H., Girard, T., Burgdorf, M., 2000. The 2.4–45 μm spectrum of Mars observed with the Infrared Space Observatory. *Planet. Space Sci.* 48, 1393–1405.
- Lewis, S.R., Collins, M., Read, P.L., Forget, F., Hourdin, F., Fournier, R., Hourdin, C., Talagrand, O., Huot, J.-P., 1999. A climate database for Mars. *J. Geophys. Res.* 104, 24177–24194.
- Melchiorri, R., Encrenaz, T., Fouchet, T., Drossart, P., Lellouch, E., Gondet, B., Bibring, J.-P., Langevin, Y., Schmitt, B. Titov, D., Ignatiev N., 2006. Water vapor mapping on Mars using OMEGA/Mars express. *Planet. Space Sci.* in press.
- Montmessin, F., Forget, F., Rannou, P., Cabane, M., Haberle, R.M., 2004. Origin and role of water ice clouds in the Martian water cycle as inferred from a general circulation model. *J. Geophys. Res.* 109, E10004. doi:10.1029/2004JE002284.
- Novak, R.E., Mumma, M.J., DiSanti, M.A., Russo, N.D., Magee-Sauer, K., 2002. Mapping of

- Ozone and Water in the Atmosphere of Mars near the 1997 Aphelion. *Icarus* 158, 14-23.
- Pearl, J.C., Smith, M.D., Conrath, B.J., Bandfield, J.L., Christensen, P.R., 2001. Observations of Martian ice clouds by the Mars Global Surveyor Thermal Emission Spectrometer: The first Martian year. *J. Geophys. Res.* 106, 12325-12338.
- Pollack, J.B., Dalton, J.B., Grinspoon, D., Wattson, R.B., Freedman, R., Crisp, D., Allen, D.A., Bézard, B., de Bergh, C., Giver, L.P., Ma, Q., Tipping, R., 1993. Near-infrared light from Venus' nightside: A spectroscopic analysis. *Icarus* 103, 1-42.
- Richardson, M.I., Wilson, R.J., 2002. Investigation of the nature and stability of the Martian seasonal water cycle with a general circulation model. *J. Geophys. Res.* 107, 5031, doi:10.1029/2001JE001536.
- Rizk, B., Wells, W.K., Hunten, D.M., Stoker, C.R., Freedman, R.S., Roush, T., Pollack, J.B., Haberle, R.M., 1991. Meridional Martian water abundance profiles during the 1988-1989 season. *Icarus* 90, 205-213.
- Rodin, A.V., Korablev, O.I., Moroz, V.I., 1997. Vertical Distribution of Water in the Near-Equatorial Troposphere of Mars: Water Vapor and Clouds. *Icarus* 125, 212-229.
- Rosenqvist, J., Drossart, P., Combes, M., Encrenaz, T., Lellouch, E., Bibring, J.P., Erard, S., Langevin, Y., Chassefière, E., 1992. Minor constituents in the Martian atmosphere from the ISM/Phobos experiment. *Icarus* 98, 254-270.
- Smith, D. E., and 23 colleagues 2001a. Mars Orbiter Laser Altimeter: Experiment summary after the first year of global mapping of Mars. *J. Geophys. Res.* 106, 23689-23722.
- Smith, M. D. 2002. The annual cycle of water vapor on Mars as observed by the Thermal Emission Spectrometer. *J. Geophys. Res.* 107, 5115. doi:10.1029/2001JE001522.
- Smith, M.D. 2004. Interannual variability in TES atmospheric observations of Mars during 1999-2003. *Icarus* 167, 148-165.
- Smith, M.D., J.L. Bandfield, and P.R. Christensen 2000. Separation of atmospheric and surface spectral features in Mars Global Surveyor Thermal Emission Spectrometer (TES) spectra. *J. Geophys. Res.* 105, 9589-9608.

- Smith, M.D., Pearl, J.C., Conrath, B.J., Christensen, P.R., 2001b. One Martian year of atmospheric observations by the Thermal Emission Spectrometer. *Geophys. Res. Letters* 28, 4263-4266.
- Spinrad, H., Münch, G., Kaplan, L.D., 1963. Letter to the Editor: the Detection of Water Vapor on Mars. *Astrophys. J.* 137, 1319-1321.
- Sprague, A.L., Hunten, D.M., Doose, L.R., Hill, R.E., Boynton, W.V., Smith, M.D., Pearl, J.C., 2006. Mars atmospheric water vapor abundance: 1991–1999, emphasis 1998–1999. *Icarus* 184, 372-400.
- Sprague, A.L., Hunten, D.M., Doose, L.R., Hill, R.E., 2003. Mars atmospheric water vapor abundance: 1996-1997. *Icarus* 163, 88-101.
- Sprague, A.L., Hunten, D.M., Hill, R.E., Doose, L.R., Rizk, B., 2001. Water Vapor Abundances over Mars North High Latitude Regions: 1996-1999. *Icarus* 154, 183-189.
- Sprague, A.L., Hunten, D.M., Hill, R.E., Rizk, B., Wells, W.K., 1996. Martian water vapor, 1988-1995. *J. Geophys. Res.* 101, 23229-23254.
- Titov, D.V. 2002. Water vapour in the atmosphere of Mars. *Adv. Space Res.* 29, 183-191.
- Titov, D.V., Moroz, V.I., Grigoriev, A.V., Rosenqvist, J., Combes, M., Bibring, J.-P., Arnold, G., 1994. Observations of water vapour anomaly above Tharsis volcanoes on Mars in the ISM (Phobos-2) experiment. *Planet. Space Sci.* 42, 1001-1010.
- Titov, D.V., Markiewicz, W.J., Thomas, N., Keller, H.U., Sablotny, R.M., Tomasko, M.G., Lemmon, M.T., Smith, P.H., 1999. Measurements of the atmospheric water vapor on Mars by the Imager for Mars Pathfinder. *J. Geophys. Res.* 104, 9019-9026.
- Zasova, L., and 20 colleagues 2005. Water clouds and dust aerosols observations with PFS MEX at Mars. *Planet. Space Sci.* 53, 1065-1077.

Table 1: Correlation of water columns with pressure

Selection	Sperman's correlation (r_s)	zd^1	Linear fit
All orbits, abs. water	0.175	23.8	$\text{H}_2\text{O} = 7.2 + 4.4 \times 10^{-3}p$
$L_s = 330^\circ - 60^\circ$, abs. water	0.532	35.8	$\text{H}_2\text{O} = 3.1 + 6.0 \times 10^{-3}p$
$L_s = 90^\circ - 180^\circ$, abs. water	0.446	52.6	$\text{H}_2\text{O} = 4.0 + 12.2 \times 10^{-3}p$
All orbits, norm. water	-0.433	59.0	$\text{H}_2\text{O} = 18.9 - 14.0 \times 10^{-3}p$
$L_s = 330^\circ - 60^\circ$, norm. water	-0.382	25.7	$\text{H}_2\text{O} = 10.4 - 5.5 \times 10^{-3}p$
$L_s = 90^\circ - 180^\circ$, norm. water	-0.298	35.2	$\text{H}_2\text{O} = 17.4 - 9.6 \times 10^{-3}p$

¹ Number of standard deviations at which the sum-squared difference of ranks deviates from its null-hypothesis expected value

Figure captions

Fig. 1: The sub-instrument local times as a function of L_s for the observations presented in this paper.

Fig. 2. Example of fits of PFS spectra in the region of H₂O rotational lines and CO₂ ν_2 band. Examples are chosen to illustrate two very different seasonal and surface temperature conditions.

Fig. 3: Effect of the water vertical profile on the retrieved water column density: example of orbit #1023 ($L_s = 111^\circ$).

Fig. 4: Seasonal distribution of water. (a, upper panel) Entire dataset; (b, lower panel) Zoom on $L_s = 90^\circ$ – 180° range. Note that the color scales are different.

Fig. 5: Comparison of water columns retrieved from PFS/LW and TES for measurements in common epoch. Left panel: original TES retrievals. Right panel: corrected TES retrievals, using the new version of the TES database (M. Smith, priv. comm.), and a further downward 15% correction (see text for details).

Fig. 6: Geographical distribution of water. Water columns are here normalized to a common 610 Pa pressure. Top left: entire dataset. Top right: $L_s = 330^\circ$ – 60° . Bottom left: $L_s = 90^\circ$ – 150° . Bottom right: $L_s = 155^\circ$ – 210° .

Fig. 7 Left: map of water vapor columns (normalized to the 610 Pa level) predicted by the LMD Global Climate Model, averaged over the period $L_s = 180^\circ$ – 210° and local times between 8 am and 4 pm. Right: the same map with superimposed streamlines illustrating the mean atmospheric transport at 3 km above the surface.

Fig. 8 Left: Longitudinal cross sections of the mixing ratio of water vapor (color-coded, mol/mol, multiply by 10^5) and water ice (black contours, mol/mol, multiply by 10^5), averaged over the period $L_s = 180^\circ$ – 210° and local times between 8 am and 4 pm at 0° N. Right: Map of water vapor volume mixing ratio predicted by the LMD Global Climate Model at 20 km above Mars zero level, averaged over the period $L_s = 180^\circ$ – 210° and local times between 8 am and 4 pm. Superimposed are streamlines illustrating the mean atmospheric circulation at the same altitude.

Fig. 9 : Water columns retrieved above the retreating north polar cap along orbit 685 ($L_s = 68.6^\circ$). Upper panel: absolute water columns; middle panel: water columns normalized to 610 Pa; lower panel: retrieved surface temperature.

Fig. 10. Absolute water columns and water volume mixing ratios below the saturation level (in part per million) in the region of three large volcanos. Olympus Mons (orbit 37), Elyseum Mons (orbit 925) and Ascraeus Mons (orbit 370). The thin lines represent the topography (arbitrary scale).

Fig. 11: Absolute (left panels) and normalized to 610 Pa (right panels) water columns vs. surface pressure. Individual measurements at latitudes between $\pm 30^\circ$ with relative error bars $< 20\%$ are displayed. Top panels: all data. Middle panels: $L_s = 330^\circ$ – 60° . Bottom panels: $L_s = 90^\circ$ – 200° . Dashed lines indicate best fits in the form $\text{H}_2\text{O} = a + b \times p_{surf}$ (see text and Table I). The solid line in the left panels show the best fits obtained by assuming proportionality of the water columns to pressure.

Fig. 12 Normalized water columns vs. surface pressure as predicted by the LMD GCM for the period $L_s = 90^\circ$ – 200° . The calculations correspond point-by-point to the observed times

and locations (i.e. to the data points of the lower panel of Fig. 11).

ACCEPTED MANUSCRIPT

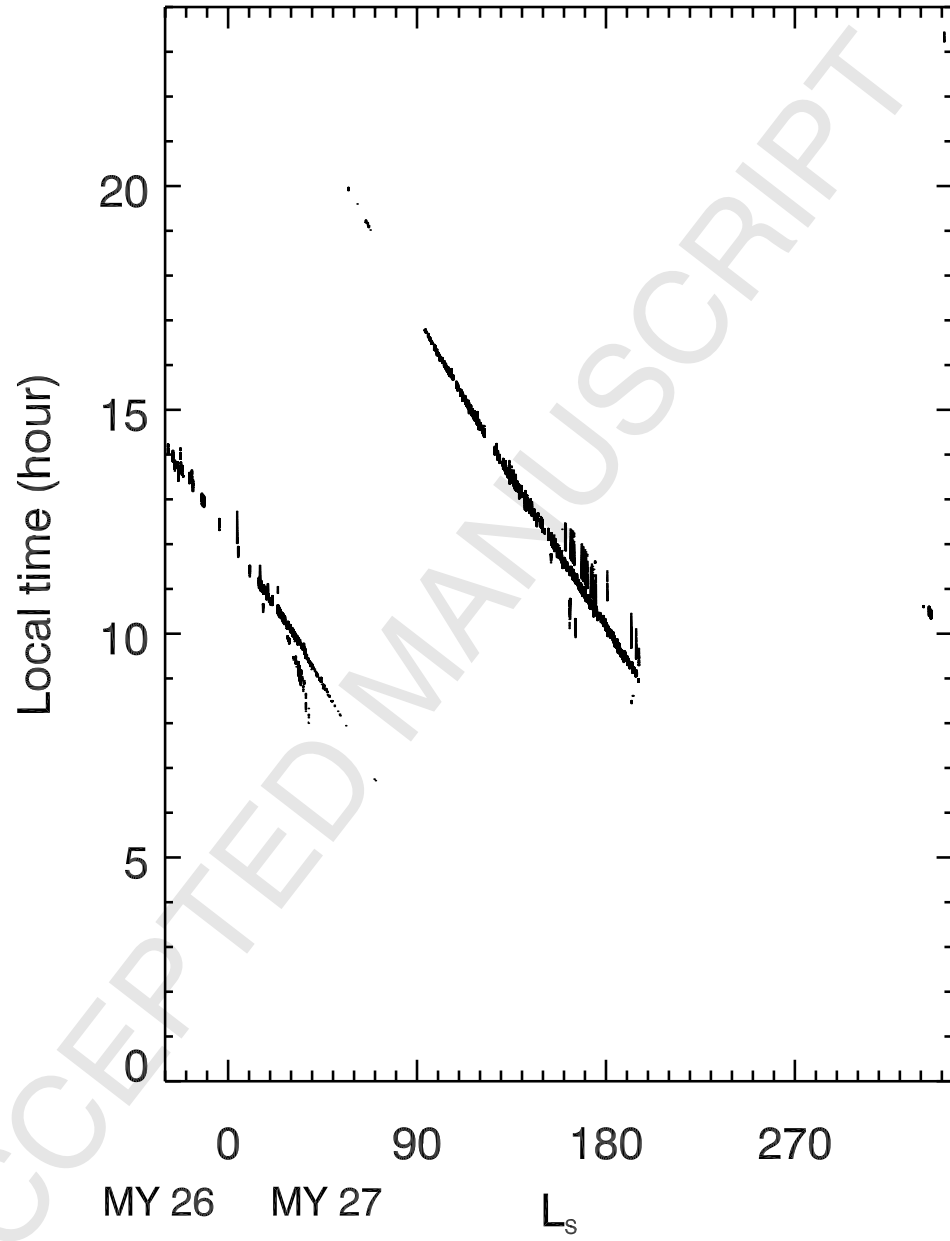


Figure 1:

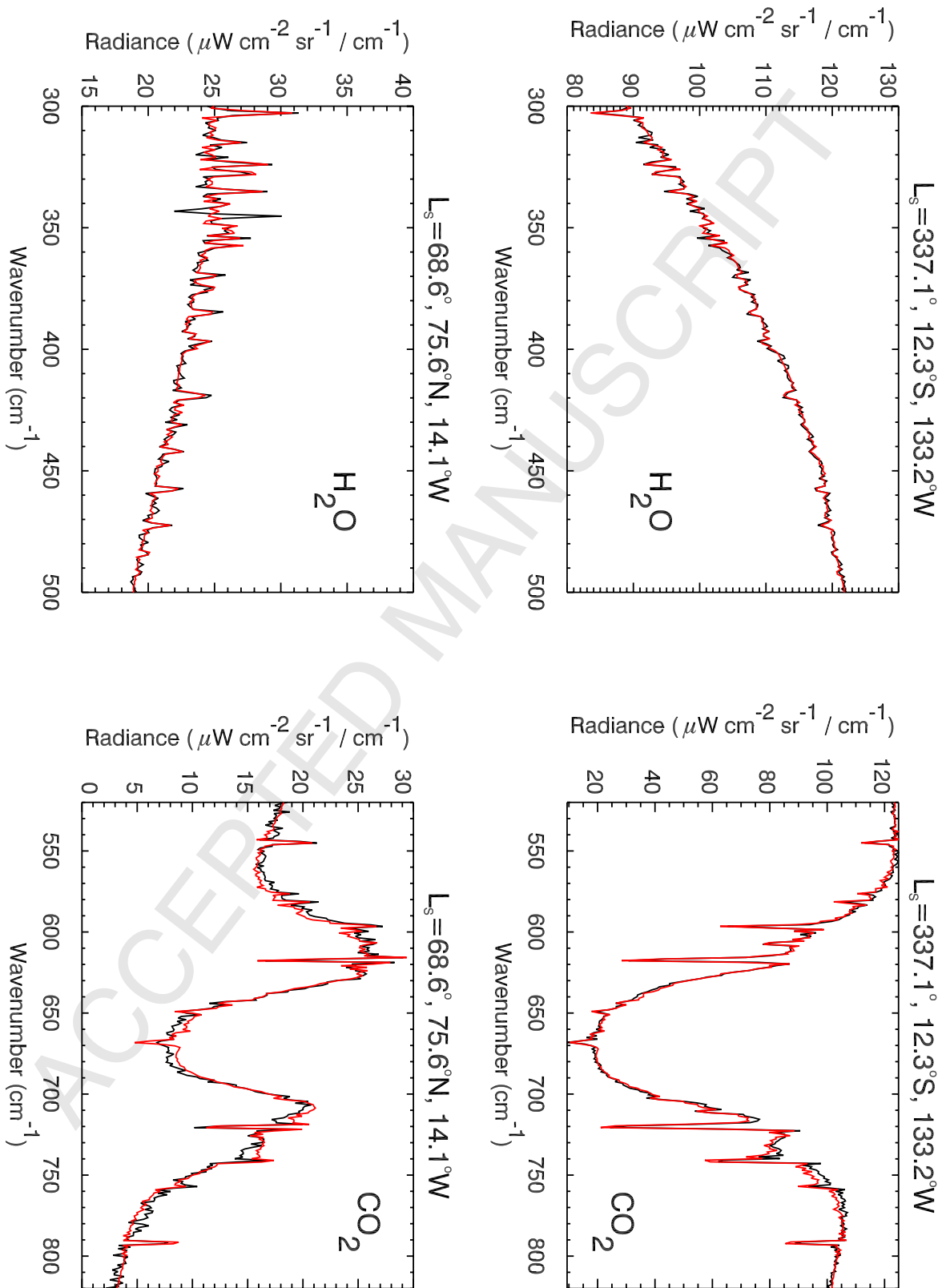


Figure 2:

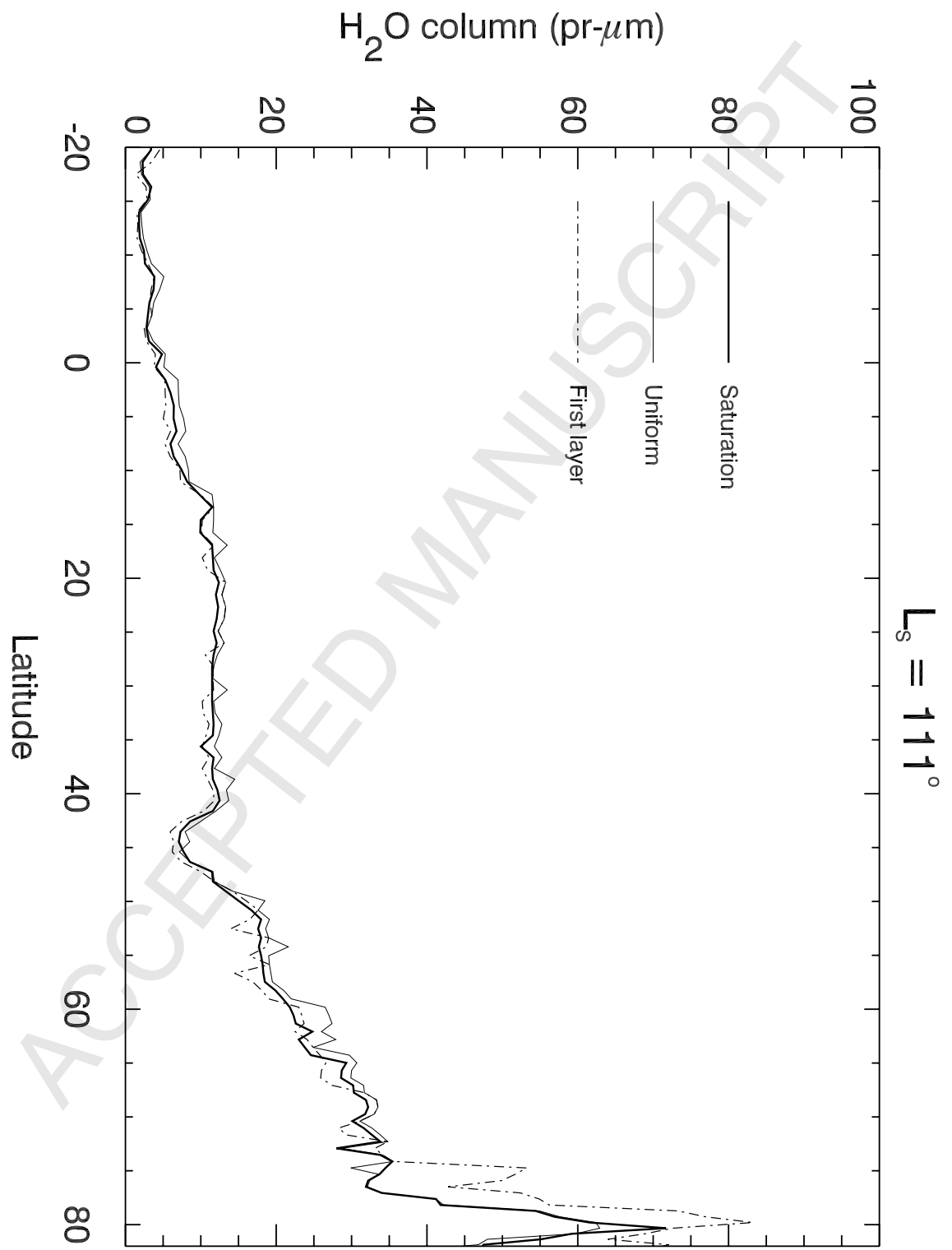


Figure 3:

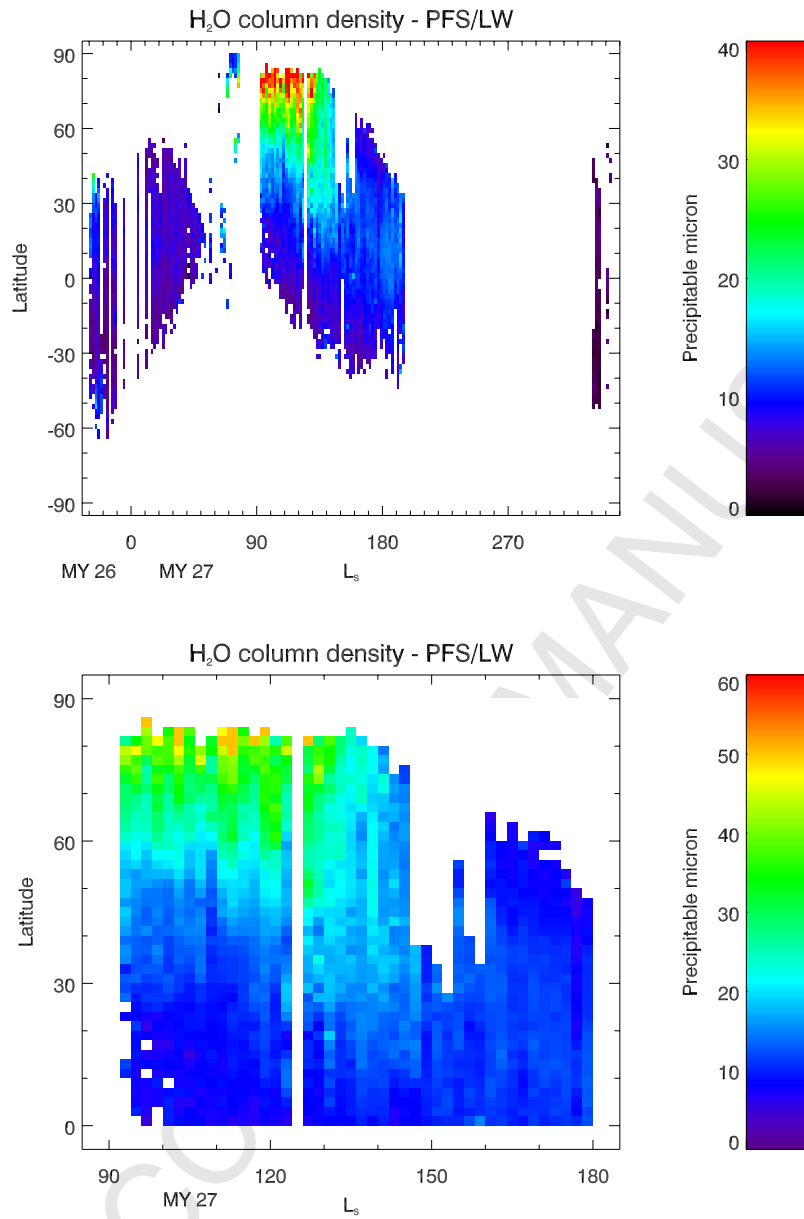


Figure 4:

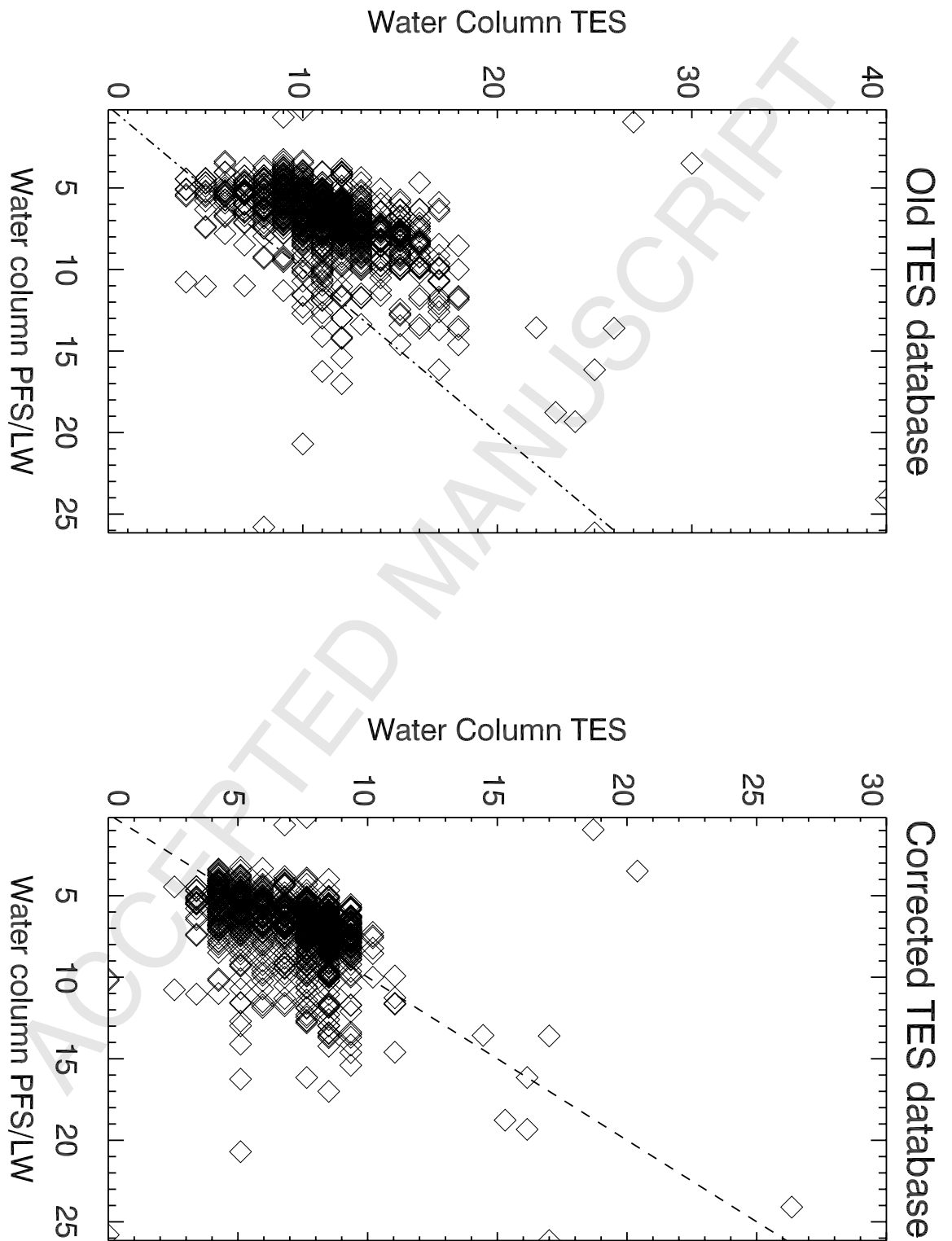


Figure 5:

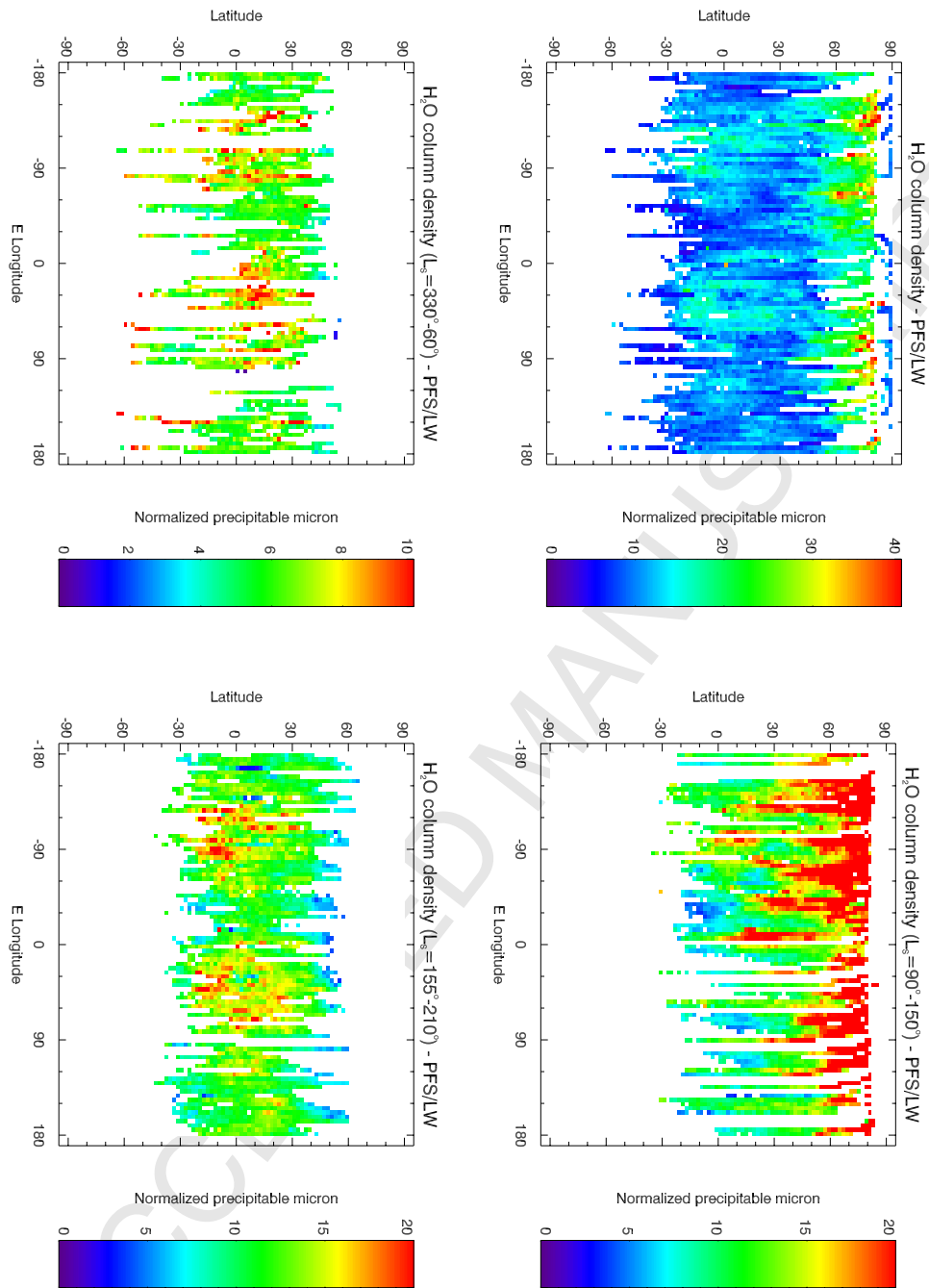


Figure 6:

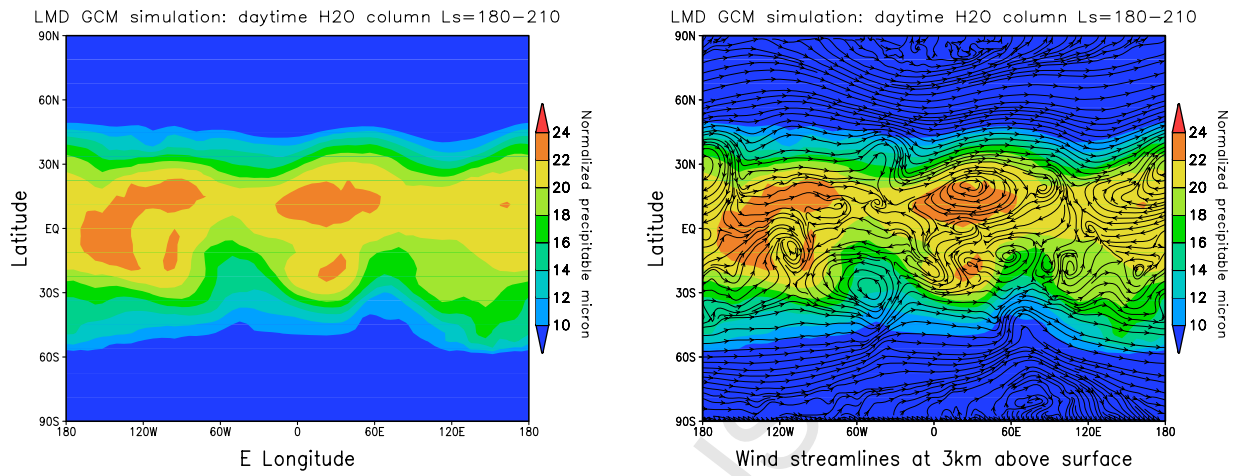


Figure 7:

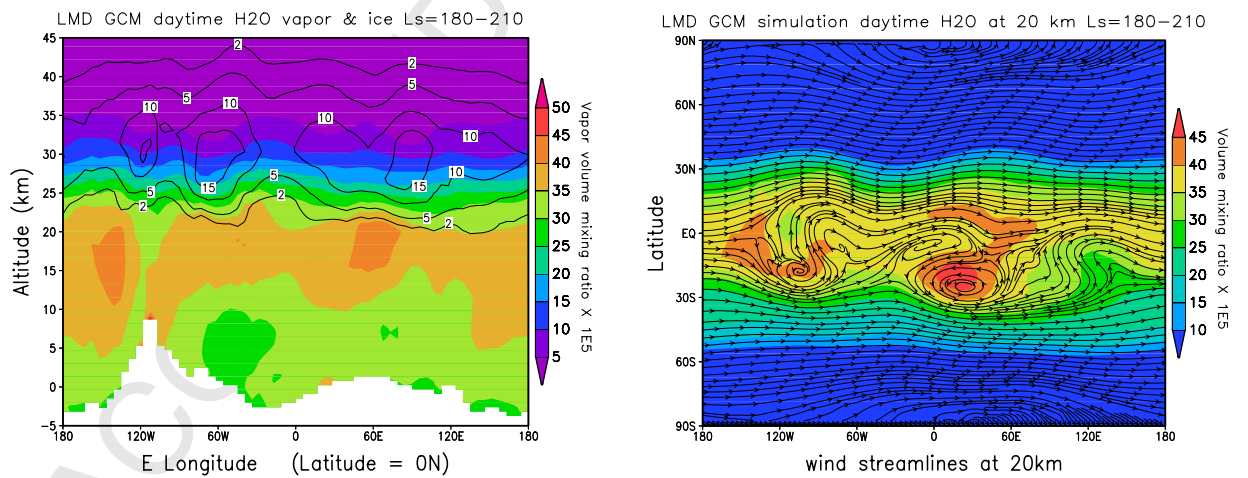


Figure 8:

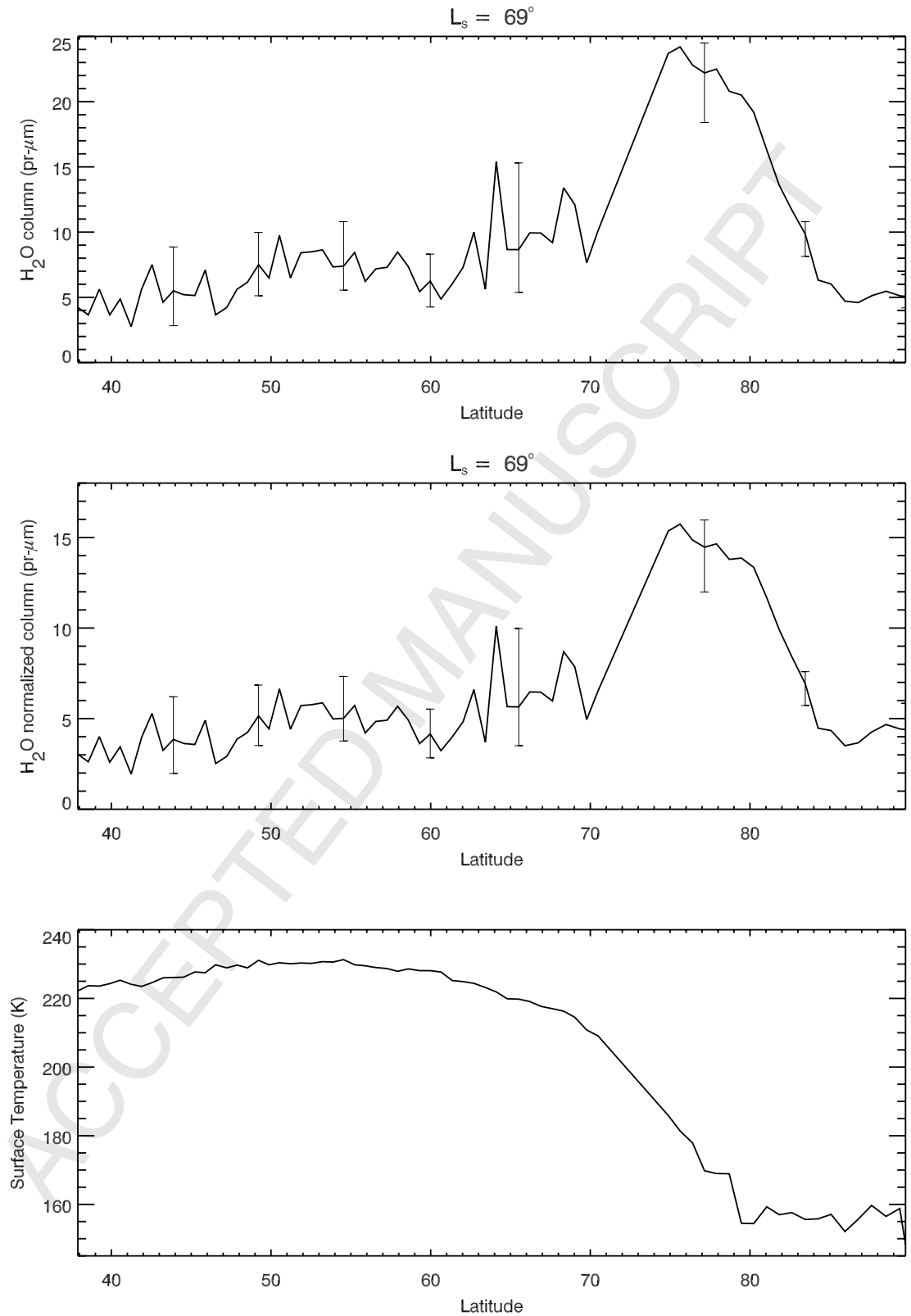


Figure 9:

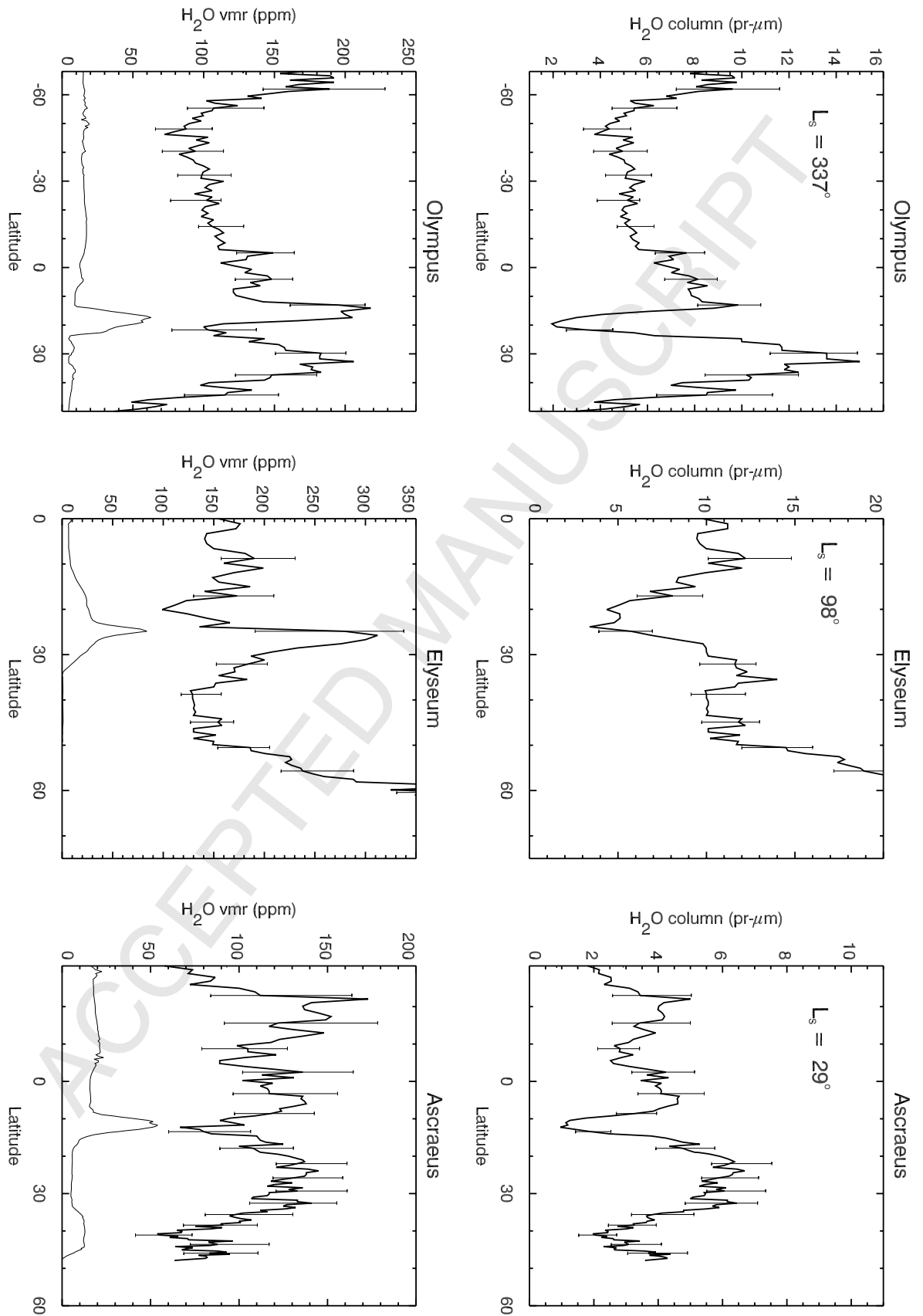


Figure 10:

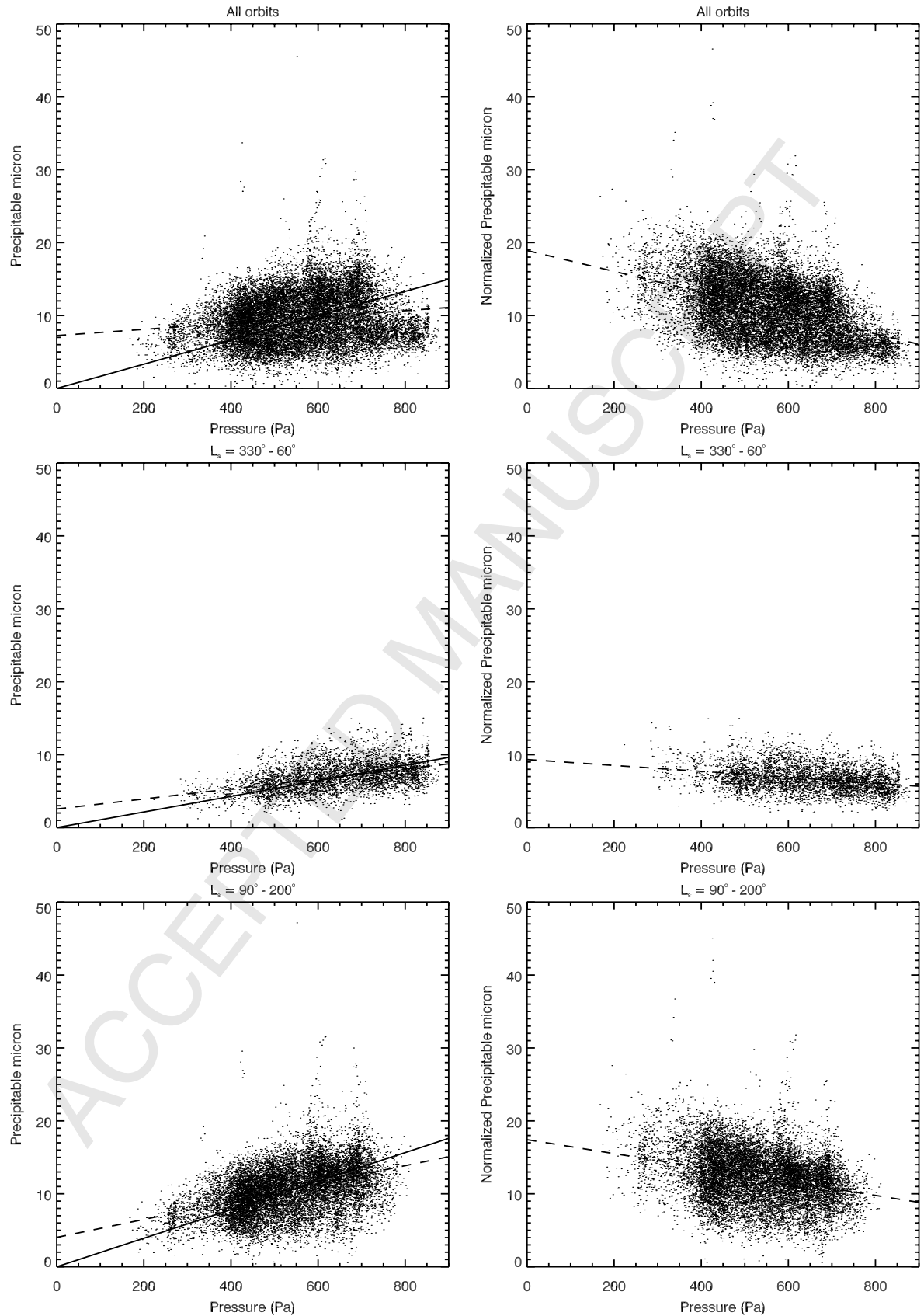


Figure 11:

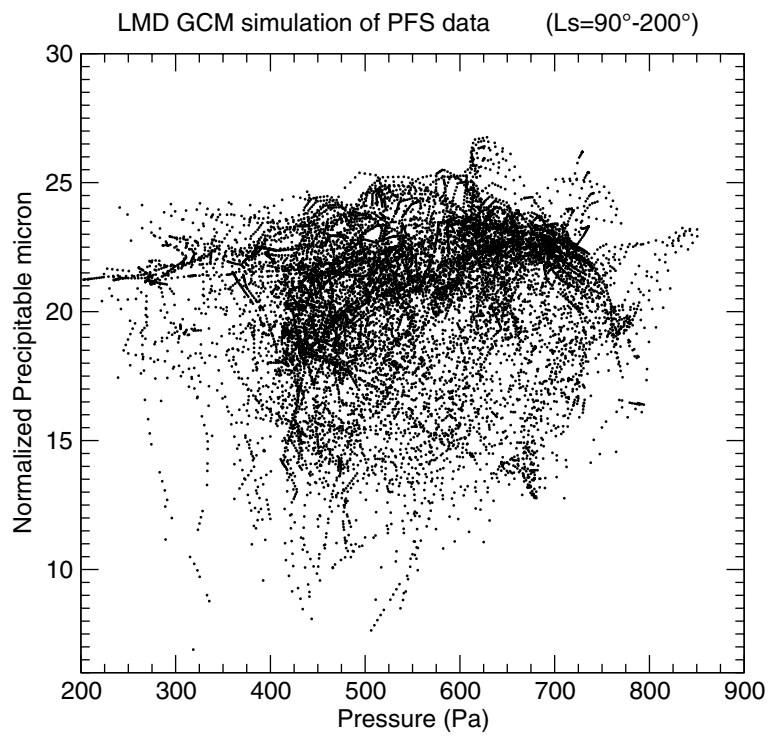


Figure 12: